工學博士學位論文

Fabrication of Shape-Controlled Inorganic Nanomaterials for Enhanced Light Absorption in Solar Cells

형태가 제어된 무기 나노소재 제조 및 태양전지 내 광흡수 향상

2016年 8月

서울大學校 大學院

化學生物工學部

盧 鐘 旻

Fabrication of Shape-Controlled Inorganic Nanomaterials for Enhanced Light Absorption in Solar Cells

by

Jongmin Roh

Submitted to the Graduate School of Seoul National University in

Partial Fulfillment of the Requirements

for the Degree of Doctor of Philosophy

August, 2016

Thesis Adviser: Jyongsik Jang

ABSTRACT

Photovoltaic (PV) devices can effectively convert sunlight into clean electrical power and provide a virtually unlimited supply of usable energy that is sustainable and environmentally benign in operation. Nanomaterials open up new possibilities to achieve higher solar energy conversion efficiencies at lower fabrication costs, as they allow the use of inexpensive materials and processing technologies to harvest sunlight by efficiently capturing photon energy over a broad spectral range, and then quickly separating and collecting photo-generated charge carriers. However, the bandgap energy of the semiconductors places a fundamental upper limit on solar energy conversion efficiency for solar cells, known as Shockley-Queisser limit which restricts the efficiency to a maximum of about 31% for unconcentrated sunlight irradiation, using a semiconductor material with an optimized band-gap of around 1.35 eV.

This dissertation describes the fabrication of shape-controlled inorganic nanomaterials for effective light harvesting in solar cells. CeO_2:Eu^{3+} nano-octahedra were prepared using a simple hydrothermal method and introduced to the TiO_2 layer of the photoanode in a dye-

sensitized solar cell (DSSC) device. The as-synthesized CeO_2:Eu^{3+} nano-octahedra possess the dual functionality of light scattering and downconversion luminescent properties, leading to increased photocurrent in DSSCs. $NaYF_4$:Yb^{3+}, Er^{3+} hexagonal nanoprisms were fabricated *via* a simple hydrothermal process. $NaYF_4$:Yb^{3+}, Er^{3+} hexagonal nanoprisms were introduced to the TiO_2 mesoporous layer in a perovskite solar cell (PSC) device as upconverting centers. Size-controlled Ag@SiO_2 nanoplates were synthesized by seed-mediated growth method and sol-gel reaction. After introduction of Ag@SiO_2 nanoplates in PSC, photocurrent was considerably increased by localized surface plasmon resonance (LSPR) effect of Ag@SiO_2 nanoplates.

The nanomaterials presented in this dissertation could be applied to various photovoltaic fields such as DSSC, PSC, and organic photovoltaic (OPV). In addition, this dissertation might not only provide a facile synthetic route for shape-controlled inorganic nanomaterials but also offer an understanding of efficient light harvesting for high-performance PV devices.

Keywords: Light absorption; inorganic nanomaterials; shape-control; photovoltaic; dye-sensitized solar cell; perovskite solar cell

Student Number: 2011-24095

List of Abbreviations

DSSC : Dye-sensitized solar cell

DRS : Diffuse reflectance spectroscopy

E_F : Fermi level

EDS : Energy dispersive X-ray spectroscopy

EIS : Electrochemical impedance spectroscopy

FE-SEM : Field emission-scanning electron microscope

FF : Fill factor

FTO : Florine-doped tin oxide

IPCE : Incident photon to converted electron

J_{SC} : Short-circuit current density

LSPR : Localized Surface plasmon resonance

MEF : Metal-enhanced fluorescence

NIR : Near-infrared

OPV : Organic photovoltaic

PCE : Power conversion efficiency

PSC : Perovskite solar cell

PV : Photovoltaic

SAED : selected area electron diffraction

SERS : Surface-enhanced Raman spectroscopy

TEM : Transmission electron microscope

UV : Ultraviolet

UV-vis : Ultraviolet-visible

V_{OC} : Open-circuit voltage

XPS : X-ray photoelectron spectroscopy

XRD : X-ray diffraction

List of Figures

Figure 1. Schematic drawing of a) light scattering within a nanocrystallite aggregate film, and b) optical reflection, refraction and absorption on/inside individual aggregates.

Figure 2. Energy-level diagram of anti-Stokes processes in $NaYF_4:Yb^{3+}$, Er^{3+}/Tm^{3+} phosphor. The sensitizer ion Yb^{3+} absorbs near-infrared (NIR) light, and the activator ions Er^{3+} or Tm^{3+} emit visible or NIR light.

Figure 3. a) Light trapping by scattering from metal nanoparticles at the surface of the solar cell. Light is preferentially scattered and trapped into the semiconductor thin film by multiple and high-angle scattering, causing an increase in the effective optical path length in the cell. b) Light trapping by the excitation of localized surface plasmons in metal nanoparticles embedded in the semiconductor. The excited particles' near-field causes the creation of electron–hole pairs in the semiconductor.

Figure 4. Energy level and device operation of dye-sensitized solar cells (DSSCs); the sensitizing dye absorbs a photon, the electron is injected into the conduction band of the TiO_2 and travels to the front electrode. The oxidized dye is reduced by the electrolyte, which is regenerated at the counter-electrode

to complete the circuit. Open circuit voltage (V_{OC}) is determined by the Fermi level (E_F) of TiO_2 and the redox potential (I^{3-}/I^-) of the electrolyte.

Figure 5. Perovskite solar cell (PSC) structure and associated vacuum energy levels for corresponding materials ($CH_3NH_3PbI_3$ perovskite, conducting TiO_2 scaffold).

Figure 6. a, b) Transmission electron microscope (TEM) images of CeO_2:Eu^{3+} nano-octahedra (1 mol% Eu^{3+}).

Figure 7. Scanning electron microscope (SEM) images of CeO_2:Eu^{3+} nano-octahedra (1 mol% Eu^{3+}).

Figure 8. The HR-TEM image of CeO_2:Eu^{3+} nano-octahedra (1 mol% Eu^{3+}).

Figure 9. The selected area electron diffraction (SAED) pattern of CeO_2:Eu^{3+} nano-octahedra (1 mol% Eu^{3+}).

Figure 10. SEM images of CeO_2:Eu^{3+} nano-octahedra with various Eu^{3+} concentrations: a) pristine CeO_2 nano-octahedra, b) 0.1 mol%, c) 0.2 mol%, d) 0.5 mol%, and e) 2 mol%.

Figure 11. X-ray diffraction (XRD) patterns of CeO_2 and CeO_2:Eu^{3+} nano-octahedra (1 mol% Eu^{3+}).

Figure 12. X-ray photoelectron spectroscopy (XPS) analysis showing b) a full scan, c) Ce 3d, and d) the Eu 3d regions of CeO_2:Eu^{3+} nano-octahedra.

Figure 13. a) UV-Vis diffuse reflectance spectra (DRS) and b) transformed Kubelka-Munk spectra of a pristine P25 film, a P25+CeO_2 (20 wt%) film, and

a P25+CeO_2:Eu^{3+} film (20 wt%, 1 mol% Eu^{3+}).

Figure 14. a) Excitation and b) emission spectra of the CeO_2:Eu^{3+} nano-octahedra for various Eu^{3+} concentrations (0.1–2 mol%).

Figure 15. Emission spectra of CeO_2:Eu^{3+} nano-octahedra (1 mol% Eu^{3+}) with N719 dye.

Figure 16. Schematic configuration of the bilayer DSSC device with CeO_2:Eu^{3+} nano-octahedra for light scattering and downconversion.

Figure 17. SEM images of a) surface morphology and cross-sectional structure of P25-CeO_2:Eu^{3+} photoanode with b) 1 layer and c) 2 layers.

Figure 18. a) Photocurrent density–voltage characteristics (*J–V* curves) of the DSSCs using P25+CeO_2 (20 wt%) film, and a P25+CeO_2:Eu^{3+} film (20 wt%, 1 mol% Eu^{3+}) and b) the dependences of J_{sc} and η on the Eu^{3+} concentration of 0.1–2 mol %.

Figure 19. Photocurrent density–voltage characteristics (*J–V* curves) of downconversion-enhanced DSSCs with increasing CeO_2:Eu^{3+} layer thickness.

Figure 20. Incident photon to converted electron (IPCE) spectra of the DSSCs using P25+CeO_2 (20 wt%) film, and a P25+CeO_2:Eu^{3+} film (20 wt%, 1 mol% Eu^{3+}).

Figure 21. Nyquist plot of downconversion-enhanced DSSCs.

Electrochemical impedance spectroscopy (EIS) measurement was performed under 100 mW cm^{-2}.

Figure 22. SEM image of $NaYF_4$:Yb^{3+}, Er^{3+} hexagonal nanoprisms.

Figure 23. XRD pattern of $NaYF_4$:Yb^{3+}, Er^{3+} hexagonal nanoprisms.

Figure 24. Upconversion photoluminescence (PL) spectrum of $NaYF_4$:Yb^{3+}, Er^{3+} hexagonal nanoprisms under 980 nm NIR laser excitation.

Figure 25. Detailed energy-level diagram and corresponding energy transitions in the $NaYF_4$:Yb^{3+}, Er^{3+} system.

Figure 26. Digital photograph of $NaYF_4$:Yb^{3+}, Er^{3+} hexagonal nanoprisms under 980 nm NIR laser excitation.

Figure 27. Schematic configuration of the PSC device with a $NaYF_4$:Yb^{3+}, Er^{3+} hexagonal nanoprism upconverting layer.

Figure 28. SEM images of TiO_2 mesoporous layer with various $NaYF_4$:Yb^{3+}, Er^{3+} hexagonal nanoprism concentrations: a) only TiO_2 nanoparticles (reference), b) TiO_2 nanoparticles with 25 wt% $NaYF_4$:Yb^{3+}, Er^{3+} nanoprisms, c) TiO_2 nanoparticles with 50 wt% $NaYF_4$:Yb^{3+}, Er^{3+} nanoprisms, and d) TiO_2 nanoparticles with 75 wt% $NaYF_4$:Yb^{3+}, Er^{3+} nanoprisms.

Figure 29. Cross-sectional SEM image of the PSC device with a $NaYF_4$:Yb^{3+}, Er^{3+} hexagonal nanoprism upconverting layer.

Figure 30. Photocurrent density–voltage (*J–V*) characteristics of PSCs using an upconverting mesoporous layer with varied ratios of $NaYF_4$:Yb^{3+}, Er^{3+} hexagonal nanoprisms.

Figure 31. The photovoltaic performance of PSCs using upconverting mesoporous layer with increasing concentration of $NaYF_4$:Yb^{3+}, Er^{3+} hexagonal nanoprisms.

Figure 32. Nyquist plots of PSCs using an upconverting mesoporous layer with varied ratios of $NaYF_4$:Yb^{3+}, Er^{3+} hexagonal nanoprisms. EIS measurements were performed under dark conditions.

Figure 33. Photocurrent density–voltage (*J–V*) characteristics of PSCs using TiO_2 nanoparticles, $NaYF_4$ hexagonal nanoprisms, and $NaYF_4$:Yb^{3+}, Er^{3+} hexagonal nanoprisms.

Figure 34. IPCE specta of PSCs using TiO_2 nanoparticles, $NaYF_4$ hexagonal nanoprisms, and $NaYF_4$:Yb^{3+}, Er^{3+} hexagonal nanoprisms.

Figure 35. The schematic diagrams of the energy transfer process in PSCs using an upconverting mesoporous layer.

Figure 36. Digital image of series of as-prepared Ag nanoplates illustrating range of colors obtained.

Figure 37. Normalized extinction spectra of series of Ag nanoplates obtained using different volumes of Ag seed solution.

Figure 38. TEM images of as-synthesized Ag nanoplates with the main LSPR peak at a) 485 nm, b) 700 nm, and c) 815 nm. TEM images of silica-coated Ag nanoplatess with the main localized surface plasmon resonance (LSPR) peak at d) 485 nm, e) 700 nm, and (f) 815 nm.

Figure 39. Normailized extinction spectra of Ag@SiO_2 nanoplates before and after silica shell coating with the main LSPR peak at a) 485 nm, b) 700 nm, and c) 815 nm.

Figure 40. Normailized extinction spectra of perovskite film and Ag@SiO_2 nanoplates with the main LSPR peak at a) 530 nm, b) 745 nm, and c) 860 nm.

Figure 41. Schematic configuration of the PSC device with size-controlled Ag@SiO_2 nanoplates.

Figure 42. Cross-sectional SEM image of the PSC device with size-controlled Ag@SiO_2 nanoplates.

Figure 43. The dependences of a) J_{sc} and b) η on the Ag nanoplates concentration of 0–1 wt% with different LSPR peaks.

Figure 44. Photocurrent density–voltage (*J–V*) characteristics of PSCs using TiO_2 nanoparticles with various Ag@SiO_2 nanoplates (0.6 wt% of Ag).

Figure 45. a) IPCE specta of PSCs using TiO_2 nanoparticles with Ag@SiO_2 nanoplates and b) the relative IPCE improvement factor spectra.

List of Tables

Table 1. Energy disperse X-ray spectroscopy (EDS) analysis of the CeO_2:Eu^{3+} nanocrystals.

Table 2. Summary of the photovoltaic properties of dye-sensitized solar cells (DSSCs) with photoanodes containing CeO_2:Eu^{3+} nano-octahedra (1 mol% Eu^{3+}). Measurements were performed under AM 1.5G sunlight intensity of 100 W cm^{-2}.

Table 3. Summary of the photovoltaic properties of DSSCs with photoanodes containing CeO_2:Eu^{3+} nano-octahedra (0.1–2 mol% Eu^{3+}).

Table 4. Summary of the photovoltaic properties of dye-sensitized solar cells (DSSCs) with different CeO_2:Eu^{3+} layer thicknesses (1 mol% Eu^{3+}).

Table 5. The average photovoltaic parameters of perovskite solar cells (PSCs) containing $NaYF_4$:Yb^{3+}, Er^{3+} and $NaYF_4$ hexagonal nanoprisms (0, 25, 50 and 75 wt%). Average values of all parameters were obtained for 15 devices.

Table 6. Photovoltaic parameters of high-performance PSCs using TiO_2 nanoparticles, $NaYF_4$ hexagonal nanoprisms, and $NaYF_4$:Yb^{3+}, Er^{3+} hexagonal nanoprisms. Measurements were performed under AM 1.5G sunlight intensity of 100 W cm^{-2}.

Table 7. Photovoltaic parameters of PSCs using TiO_2 nanoparticles, with various $Ag@SiO_2$ nanoplates (0.6 wt% of Ag). Measurements were performed under AM 1.5G sunlight intensity of 100 W cm^{-2}.

Table of Contents

Abstract ..... **i**

List of Abbreviations ..... **iv**

List of Figures ..... **vi**

List of Tables ..... **xii**

Table of Contents ..... **xiv**

1. INTRODUCTION **1**

1.1. Background **1**

1.1.1. Light absorption 1

1.1.1.1. Light scattering 1

1.1.1.2. Downconversion 4

1.1.1.3. Upconversion 6

1.1.1.4. Localized surface plasmon resonance 9

1.1.2. Application fields 14

1.1.2.1. Dye-sensitized solar cell 14

1.1.2.2. Perovskite solar cell 17

1.2. Objectives and Outlines **19**

1.2.1. Objectives 19

1.2.2. Outlines 19

2. EXPERIMENTAL DETAILS.....22

2.1. CeO_2:Eu^{3+} nano-octahedra for dye-sensitized solar cells.....22

2.1.1. Fabrication of CeO_2:Eu^{3+} nano-octahedra.....22

2.1.2. Characterization of CeO_2:Eu^{3+} nano-octahedra.....22

2.1.3. Application to dye-sensitized solar cell.....23

2.2. β-$NaYF_4$:Yb^{3+}, Er^{3+} hexagonal nanoprisms for perovskite solar cells 25

2.2.1. Fabrication of β-$NaYF_4$:Yb^{3+}, Er^{3+} hexagonal nanoprisms.25

2.2.2. Characterization of β-$NaYF_4$:Yb^{3+}, Er^{3+} hexagonal nanoprisms.....26

2.2.3. Application to perovskite solar cell 27

2.3. Size-controlled Ag@SiO_2 nanoplates for perovskite solar cells.....29

2.3.1. Fabrication of size-controlled Ag@SiO_2 nanoplates.....29

2.3.2. Characterization of size-controlled Ag@SiO_2 nanoplates...31

2.3.3. Application to perovskite solar cell 31

3. RESULTS AND DISCUSSION 34

3.1. CeO_2:Eu^{3+} nano-octahedra for dye-sensitized solar cells.....34

3.1.1. Fabrication of CeO_2:Eu^{3+} nano-octahedra.....34

3.1.2. Characterization of CeO_2:Eu^{3+} nano-octahedra.....42

3.1.3. Application to dye-sensitized solar cell.....54

3.2. β-$NaYF_4$:Yb^{3+}, Er^{3+} hexagonal nanoprisms for perovskite solar cells.....67

3.2.1. Fabrication of β-$NaYF_4$:Yb^{3+}, Er^{3+} hexagonal nanoprisms.67
3.2.2. Characterization of β-$NaYF_4$:Yb^{3+}, Er^{3+} hexagonal nanoprisms.....69
3.2.3. Application to perovskite solar cell 75
3.3. Size-controlled Ag@SiO_2 nanoplates for perovskite solar cells.....93
3.3.1. Fabrication of size-controlled Ag@SiO_2 nanoplates.....93
3.3.2. Characterization of size-controlled Ag@SiO_2 nanoplates...98
3.3.3. Application to perovskite solar cell 101

4. CONCLUSIONS.....112
REFERENCES 115
국문초록 123

1. INTRODUCTION

1.1. Background

1.1.1. Light harvesting

1.1.1.1. Light scattering

Light scattering is a common phenomenon in optics regarding the propagation of light in the presence of object. Generally, when light reaches an object, according to the laws of reflection and refraction, the incident light may either penetrate in the forward direction, giving rise to refraction and absorption, or return in the backward direction, causing reflection. However, when the dimensions of the object are on the order of the wavelength of light, the radiation will be spread in all directions that deviate from the trajectory of the reflected or refracted light as determined by the laws of reflection and refraction. Such an optical phenomenon is called light scattering, and the object that causes the light scattering is known as the scatterer or scattering material.[1]

Light scattering is an important method that has been applied to enhance the power conversion efficiency (PCE) of DSSCs.[1-3] The basic idea of a light scattering method is to confine the incident light and extend the traveling distance of light within the photoelectrode film so as to increase the opportunity of the photons to be absorbed by the

dye molecules, and in this way, to improve the light harvesting efficiency of the photoelectrode as well as the PCE of the DSSCs (**Figure 1**).

To increase the light absorption capability in DSSCs, large semiconductor microspheres (*e.g.*, TiO_2,[4, 5] ZnO,[6, 7] SnO_2,[8, 9] and CeO_2[10]), hollow microspheres,[3, 5, 11] microplates,[12] and electrospun nanofibers[13, 14] are utilized in the scattering layer to increase the optical pathlength of light. Among the semiconductor materials, CeO_2 offers an enhanced light-scattering ability for DSSCs, due to its cubic nanostructure with high refractive index for visible light and exposed mirror-like facets.[15] Specifically, it is reported that the mirror-like facets of CeO_2 significantly improve light scattering compared with curved surfaces, reflecting the incident light directly back to the photoanode.[10]

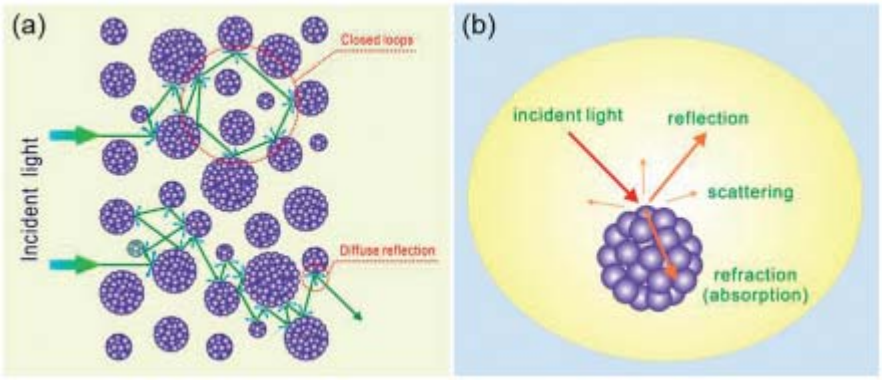

Figure 1. Schematic drawing of a) light scattering within a nanocrystallite aggregate film, and b) optical reflection, refraction and absorption on/inside individual aggregates.[16]

1.1.1.2. Downconversion

Photon downconversion is composed of two types of energy conversion processes that are useful for solar cells.[17] One is based on photon quantum cutting,[18, 19] the other one is based on Stokes-shifted emission.[20] Quantum cutting is a direct conversion of the energy of one absorbed photon into two or more emitted low-energy photons. This process is known to have quantum efficiency more than 100%.[19] Lanthanide ions which possess the ladder-like spacing of energy levels provide opportunities for a quantum cutting mechanism due to pronounced energy transfer between two lanthanide ions of the same or different types.

Stokes-shifted luminescence can be applied in solar devices where the photoactive component has a poor spectral photoresponse to short-wavelength light. A Stokes-shifting material absorbs the short-wavelength light in the 300-500 nm range, and re-emits at a longer wavelength where the external quantum efficiency of the PV device is high.[20] While Stokes-shift luminescence can increase the solar cell efficiency, it cannot overcome the Shockley-Queisser limit, as thermalization losses remain unchanged.[21] In practice, a planar Stokes-shifting layer is placed directly onto the front surface of a solar

cell to enhance the device performance by transforming short wavelength photons to longer wavelength photons at a quantum yield near unity.[22, 23] Until now, lanthanide-doped inorganic phosphors,[24-27] colloidal quantum dots,[28, 29] organolanthanide complexes,[29] organic dyes[30, 31] have been widely investigated as Stokes-shifting materials, manifesting enhanced PCEs in solar cell devices.

Europium ions (Eu^{3+}) are well known as bright red luminescent phosphors and are commonly used as activators in various inorganic host lattices.[32] In particular, downconversion photoluminescence (PL) of Eu^{3+} ions have been examined in host materials Y_2O_3,[33] $NaGdF_4$,[34] Sr_2CeO_4,[35] and CeO_2.[36-38] In the downconversion process, the incident photon is converted into two or more low-energy photons, leading to high energy conversion efficiency in solar cells.[39] CeO_2:Eu^{3+} is a promising material for improving DSSC efficiency, exhibiting excellent downconversion luminescent properties through energy transfer from the Ce^{4+}-O^{2-} charge transfer transition in the CeO_2 host to the Eu^{3+} ions.[37]

1.1.1.3. Upconversion

Photon upconversion explains anti-Stokes optical processes that convert two or more low energy photons to generate a higher energy photon by sequential absorption or ion-to-ion energy transfer.[40] This phenomenon was first discovered by Auzel in the 1960s.[41] The absorption of photons with energy higher than the bandgap can generate electron-hole pairs contributing to the electric current. Indeed, the transmission of sub-bandgap photons is one of the major energy losss in conventional solar cells. In the case of silicon solar cells, the transmission loss amounts to about 20% of the incident solar energy, which is not considerably reducible by conventional approaches.[21] To this end, the use of upconversion materials may provide a solution to the transmission loss by converting two sub-bandgap photons into one above-bandgap photon.[42-45] Indeed, Trupke et al. in 2002 showed that the theoretical efficiency limit of a single-junction solar cell, modified with an upconverter, can reach 63.2% for concentrated sunlight and 47.6% for non-concentrated sunlight, respectively.[46] Without altering the already existing merits of a solar cell, the photon upconversion approach utilizes the anti-Stokes upconversion technique to convert long wavelength light to visible photons that can

be efficiently absorbed by various solar cells.[47] The upconversion technique is realized by rare earth-doped nanocrystals.[40, 41] The upconversion process produces a highly energetic excited state in the rare earth ion by sequential absorption of two or more low energy photons.

Among many upconversion materials, ytterbium and erbium codoped beta-phase sodium yttrium fluoride (β- $NaYF_4:Yb^{3+}$, Er^{3+}) is well known as the most efficient upconversion phosphor for bright green PL and is widely used in lasers,[48, 49] solar cells,[50, 51] and bioimaging.[52, 53] In $NaYF_4:Yb^{3+}$, Er^{3+} phosphor, Yb^{3+} ions act as a near-infrared (NIR) sensitizer and Er^{3+} ions act as a visible photon emitter (**Figure 2**).[54] $NaYF_4:Er^{3+}$ upconversion phosphors, applied to the bottom layer of silicon solar cells, theoretically increase the PCE of the cells from 20% to 25%.[50] In DSSCs, large $NaYF_4:Yb^{3+}$, Er^{3+} nanoplates and nanoprisms have been utilized as upconverting and light scattering materials to increase the optical pathlength of the incident light and to obtain better NIR response.[51, 55-57] It is expected that upconversion nanomaterials can be used to improve the photovoltaic performance of PSCs, as well as silicon solar cells and DSSCs.

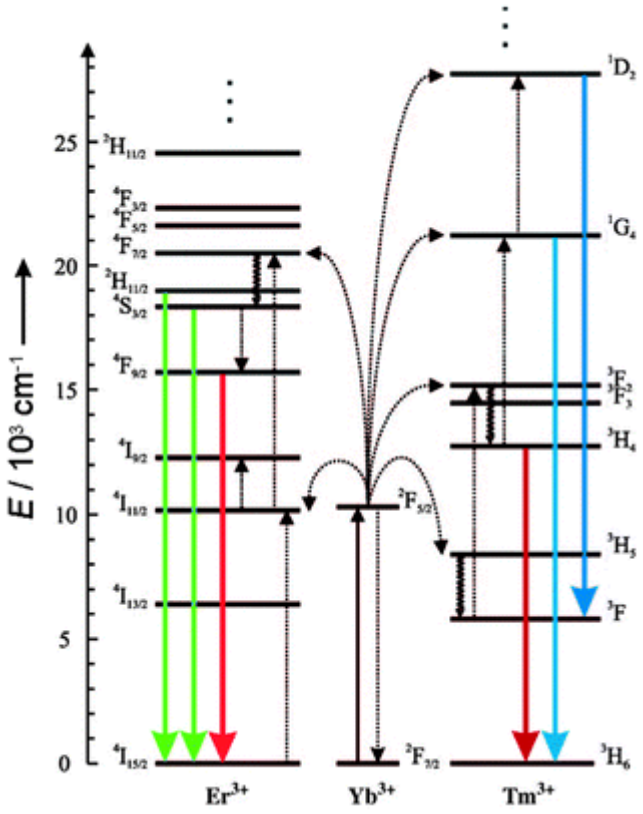

Figure 2. Energy-level diagram of anti-Stokes processes in $NaYF_4:Yb^{3+}$, Er^{3+}/Tm^{3+} phosphor. The sensitizer ion Yb^{3+} absorbs near-infrared (NIR) light, and the activator ions Er^{3+} or Tm^{3+} emit visible or NIR light.[58]

1.1.1.4. Localized surface plasmon resonance

Nanoparticles of noble metals such as silver or gold are of considerable interest in nanotechnology as plasmonic nanomaterials. Plasmonic nanomaterials possesses the unique property of the collective oscillation of the conduction electrons in resonance with certain frequencies of incident light, leading to an extinction known as a localized surface plasmon resonance (LSPR).[59-61] The spectral position of the resonance is highly dependent on nanoparticle size and shape and also depends on the refractive index of the metal with surrounding medium. An appropriate incorporation of plasmonic nanomaterials in the device can concentrate and fold the sunlight in a thin semiconductor layer, thereby increasing the sunlight absorption of solar cells by creating an increase in the optical path derived from strong plasmonically enhanced scattering. Surface plasmon polaritons propagating at the plasmonic substance/semiconductor interface are also promising for increasing the device absorption.

Plasmonic nanomaterials can offer two ways of reducing the physical thickness of the PV absorber layers, while keeping their optical thickness constant.[62] First, sunlight can be bounced into the light absorbing thin film using plasmonic nanoparticles as

subwavelength scattering elements, increasing the effective optical light pathway in the thin film (**Figure 3a**). It has been shown that when the plasmonic particles are placed close to the interface between two dielectrics, light will be preferentially scattered into the dielectric with a larger permittivity.[63] Moreover, light scattered at an angle beyond the critical angle for reflection (total internal reflection) will remain trapped in the cell. The employment of a reflecting metal back contact can reflect sunlight back to the plasmonic scatters, which enable multiple passes of scattered sunlight through the light absorbing film, providing an additional way to increase the effective path length. In addition, light-trapping effects are most pronounced at the peak of the plasmon resonance spectrum.[64] Plasmonic nanostructures with a peak near the bandgap are required for the use of scattering geometry to enhance device absorption. Tunability of the plasmonic absorption peak is needed because of the varying bandgaps of light absorbing materials in different types of solar cells.

Second, sunlight can be concentrated using plasmonic nanoparticles as sub-wavelength antennas in which the plasmonic near-field is coupled to the semiconductor, thereby, increasing its effective absorption cross-section (**Figure 3b**). Small sized (5-20 nm diameter)

particles work particularly well for this geometry, as a low fraction of the absorbed light is emitted as radiation in them.[62] These antennas are particularly useful in materials where the carrier diffusion lengths are small, and charge carriers must be generated close to the collection junction area. Incorporating small plasmonic metal nanoparticles in the active layer has resulted in enhanced efficiencies in bulk hetero-junction organic solar cells,[65] tandem polymer solar cells,[66] DSSCs,[67] as well as in silicon solar cells.[68]

Triangular silver nanoplates have attracted extensive research interest because of the unique size- and shape-dependent optical properties that arise as a result of their LSPR modes.[69, 70] Because of their relatively large size and highly anisotropic shape and the high radius of curvature of the tips, triangular silver nanoplates have a number of advantages over other plasmonactive nanoparticles. These include LSPR bands that are tunable throughout the visible and into the NIR region of the spectrum and large increases in the strength of the electric field at the particle tips as a result of near-field enhancements.[71, 72] As a result of these highly advantageous properties, silver nanoplates have a wide variety of applications, including their use as sensors,[73] in surface-enhanced Raman

spectroscopy (SERS)[74] and metal-enhanced fluorescence (MEF) experiments,[75] as contrast agents for photoacoustic imaging,[76] and in plasmon-enhanced organic electronic devices.[76]

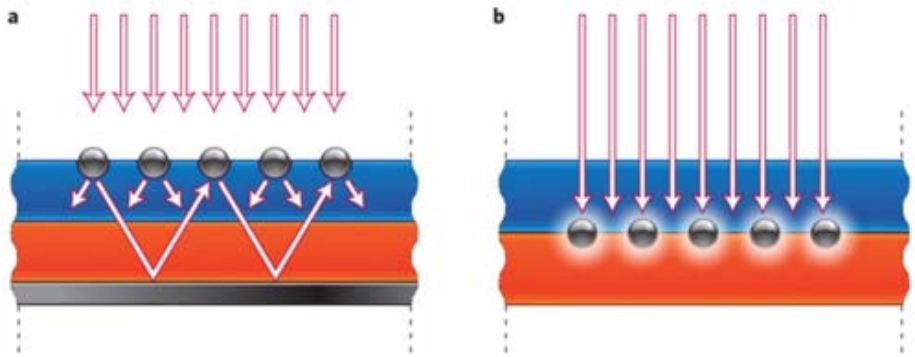

Figure 3. a) Light trapping by scattering from metal nanoparticles at the surface of the solar cell. Light is preferentially scattered and trapped into the semiconductor thin film by multiple and high-angle scattering, causing an increase in the effective optical path length in the cell. b) Light trapping by the excitation of localized surface plasmons in metal nanoparticles embedded in the semiconductor. The excited particles' near-field causes the creation of electron–hole pairs in the semiconductor.[62]

1.1.2. Application fields

1.1.2.1. Dye-sensitized solar cell

As global demands for energy increase, photovoltaics have been recognized as a clean, renewable energy source. Since its introduction in 1991, the DSSC is considered particularly promising, due to its low cost, easy production, and relatively high efficiency.[77, 78] Conventional DSSC photoanodes are generally based on a mesoporous network of TiO_2 nanoparticles upon which dye molecules are absorbed for light harvesting.[79] With light absorption, photoexcited electrons in the dyes are injected into the conduction band of the TiO_2 network (**Figure 4**).[80] From this viewpoint, the properties of the semiconductor materials and dyes in the photoanode have a direct effect on the efficiency of the DSSC. However, TiO_2 nanoparticles give rise to a considerable loss of incident light due to the transmission of light through the photoanode.[4, 81] Moreover, Ru-based dyes commonly used in DSSCs (*e.g.*, N719, N749, and N3) have a narrow absorption spectral range in the visible regime, resulting in an energy loss of the incident light for ultraviolet (UV) and NIR wavelengths.[82] Therefore, high-performance DSSC photoanodes, capable of increasing light absorption and extending the

light absorption range, are required to improve the existing conventional DSSC configuration.

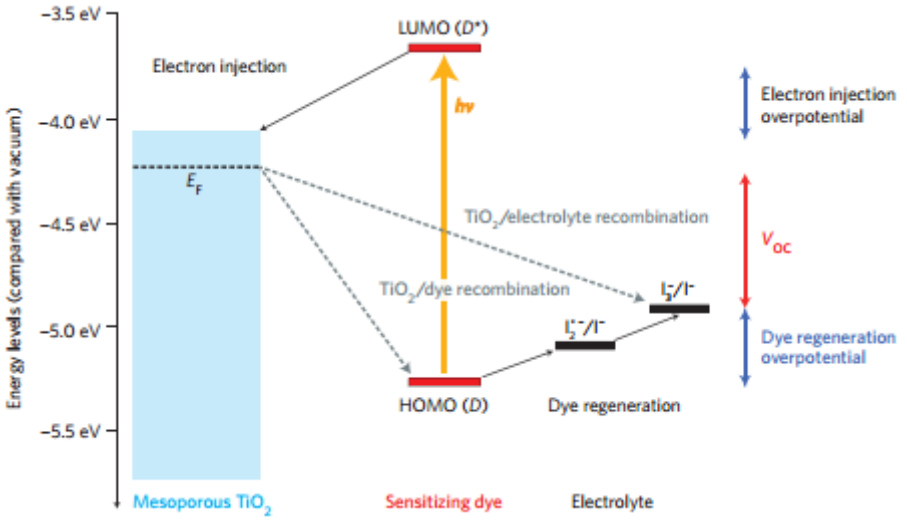

Figure 4. Energy level and device operation of dye-sensitized solar cells (DSSCs); the sensitizing dye absorbs a photon, the electron is injected into the conduction band of the TiO_2 and travels to the front electrode. The oxidized dye is reduced by the electrolyte, which is regenerated at the counter-electrode to complete the circuit. Open circuit voltage (V_{OC}) is determined by the Fermi level (E_F) of TiO_2 and the redox potential (I^{3-}/I^-) of the electrolyte.[83]

1.1.2.2. Perovskite solar cell

Organolead trihalide perovskite ($CH_3NH_3PbX_3$, X = Cl, Br, I) is considered to be a particularly promising material, due to its unique properties that include a large absorption coefficient,[84] ambipolar charge transport,[85] long electron–hole diffusion lengths,[86, 87] and facile solution processability.[88-90] Since organolead trihalide perovskite was rediscovered as the sensitizer in solid-state solar cells,[91] PSCs have increasingly improved their PCE, rising from 9.7%[91] to 20.1%.[92] To date, there have been numerous attempts to improve the photovoltaic performance and stability of PSC devices, such as by controlling the processing conditions of perovskite films,[93, 94] engineering the chemical composition of perovskite,[95, 96] introducing additives to perovskite,[97] and designing interface energy alignments.[98, 99] However, the perovskite sensitizer has a bandgap of 1.55 eV and absorbs only a small portion of incident light in the visible spectrum (up to 800 nm),[91, 100] thus resulting in energy loss due to the non-absorption of NIR light. Light harvesting of low-energy photons below the absorption threshold of perovskite is required for high-performance PSC devices.

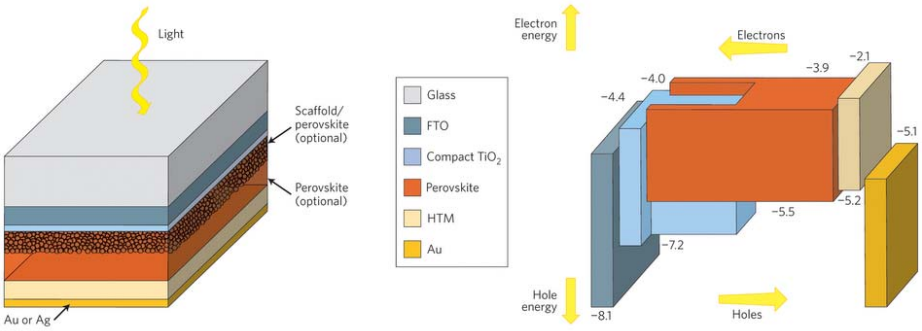

Figure 5. Perovskite solar cell (PSC) structure and associated vacuum energy levels for corresponding materials ($CH_3NH_3PbI_3$ perovskite, conducting TiO_2 scaffold).[84]

1.2 Objectives and Outlines

1.2.1 Objectives

The aim of this dissertation is providing fabrication methods of inorganic nanomaterials to improve light absorption capability in solar cells. Particularly, $CeO_2:Eu^{3+}$ nano-octahedra, β-$NaYF_4:Yb^{3+}$, Er^{3+} hexagonal nanoprisms, and size-controlled $Ag@SiO_2$ nanoplates were synthesized. Finally, these prepared nanomaterials were applied to the photovoltaic devices such as DSSCs and PSCs.

1.2.2. Outlines

This dissertation focused on the fabrication of light harvesting inorganic nanomaterials and applications in photovoltaic field. This dissertation involves the following subtopics:

I. $CeO_2:Eu^{3+}$ nano-octahedra for dye-sensitized solar cells

II. β-$NaYF_4:Yb^{3+}$, Er^{3+} hexagonal nanoprisms for perovskite solar cells

III. Size-controlled $Ag@SiO_2$ nanoplates for perovskite solar cells

A detailed outline of the study is as follows:

1. Dual-functional CeO_2:Eu^{3+} nano-octahedra were prepared using a simple hydrothermal method, possessing both light-scattering and downconversion luminescent properties. A CeO_2:Eu^{3+} layer was introduced to the TiO_2 layer of the photoanode in a DSSC device. The as-synthesized CeO_2:Eu^{3+} nano-octahedra are large in size (300–400 nm) and have mirror-like facets that facilitate light scattering. Additionally, the CeO_2:Eu^{3+} nano-octahedra broadened the absorption range of the DSSC *via* downconversion luminescence, which in turn, increased the photocurrent.

2. β-$NaYF_4$:Yb^{3+}, Er^{3+} hexagonal nanoprisms were fabricated via a simple hydrothermal process. $NaYF_4$:Yb^{3+}, Er^{3+} hexagonal nanoprisms were introduced to the TiO_2 mesoporous layer in a PSC device as upconverting centers. Low-energy NIR light absorbed by $NaYF_4$:Yb^{3+}, Er^{3+} hexagonal nanoprisms cores can be converted into high-energy visible light that can be utilized in PSCs. Thus, the $NaYF_4$:Yb^{3+}, Er^{3+} hexagonal nanoprisms expand the absorption range of the PSC *via* upconversion PL, resulting in an enhancement of the photocurrent.

3. Size-controlled Ag nanoplates were fabricated using a seed-mediated growth method and SiO_2 shell was coated on Ag nanoplate

via a Stöber reaction. $Ag@SiO_2$ nanoplates were incorporated into the TiO_2 mesoporous layer in a PSC device for plasmon-enhanced light absorption. Due to the LSPR effect of the size-controlled $Ag@SiO_2$ nanoplates, the light absoption near the LSPR peak was considerably improved, leading to an enhancement of the photocurrent and PCE.

2. EXPERIMENTAL DETAILS

2.1. $CeO_2:Eu^{3+}$ nano-octahedra for dye-sensitized solar cells

2.1.1. Fabrication of $CeO_2:Eu^{3+}$ nano-octahedra

CeO_2 and $CeO_2:Eu^{3+}$ nano-octahedra were synthesized using a hydrothermal process. Typically, 2 g cerium(III) nitrate hexahydrate, 0.02–0.4 g europium(III) nitrate pentahydrate, and 7.6 mg trisodium phosphate dodecahydrate were added to 80 mL of distilled water and stirred for 1 h. The mixture was then transferred to a 100 mL Teflon-lined stainless steel autoclave and heated at 180°C for 12 h. Precipitates were collected by centrifugation, washed with water and ethanol, and then dried in an oven.

2.1.2. Characterization of $CeO_2:Eu^{3+}$ nano-octahedra

The morphology of the CeO_2 and $CeO_2:Eu^{3+}$ nano-octahedra was observed by energy-filtering transmission electron microscopy (EF-TEM, Carl Zeiss LIBRA 120), high-resolution transmission electron microscopy (HR-TEM), and selected-area electron diffraction (SAED) (JEOL JEM-3010). Field-emission scanning electron microscopy (FE-SEM) and energy-dispersive X-ray spectroscopy (EDS) data were obtained with a JEOL 6700. X-ray diffraction (XRD) was performed

using a Bruker New D8 Advance with a Cu-Kα radiation source (λ: 1.5406 Å) at 40 kV and 300 mA (12 kW). X-ray photoelectron spectroscopy (XPS) was carried out with a SIGMA PROVE (ThermoVG). A Lambda 35 (Perkin-Elmer) UV-Vis spectrometer was used for absorption measurements and diffuse reflectance spectroscopy (DRS). The band gap energy can be determined the plot of Kubelka-Munk fuction, $[F(R)h\nu]^{1/2} = A(h\nu - E_g)$ versus incident photon energy. F(R) is the optical absorption coefficient which is calculated using reflectance data, $F(R) = (1 - R)^2/2R$. E_g is the band gap energy and A is the constant depending on transition probability.[37] All PL spectra were measured on a JASCO FP-6500 spectrofluorometer. The PL intensity of excitation/emission was investigated with increasing Eu^{3+} content over the wavelength ranges of 200–450 nm (λ_{ex} = 590 nm) and 550–700 nm (λ_{ex} = 330 nm).

2.1.3. Application to dye-sensitized solar cell

The screen-printable P25 paste was prepared by adding ethyl cellulose, lauric acid, and terpineol to an ethanol solution of P25 particles, followed by stirring and sonication. The ethanol was removed using a rotary evaporator. The paste was then mixed using a 3-roll mill

to create a homogeneous mixture. The nominal composition of P25/terpineol/ethyl cellulose/lauric acid was 1/3.3/0.5/0.3. FTO glass was cleaned by sonication in distilled water, acetone, and 2-propanol for 60 min each, followed by pretreatment with 40 mM $TiCl_4$ solution before being heated at 450°C for 30 min. The P25 paste was coated onto the FTO glass by successive screen-printing. To prepare a CeO_2:Eu^{3+} dual-functional layer, the P25 paste with 20 wt% CeO_2:Eu^{3+} nano-octahedra was mixed using a mortar and pestle. The mixed P25/CeO_2:Eu^{3+} paste was then screen-printed onto the P25 film, which was sintered at 450°C for 30 min. The photoanode was then treated with 40 mM $TiCl_4$ and sintered at 450°C for 30 min. The prepared films (area: 0.16 cm^2) were soaked in N719 dye solution (5×10^{-4} M in absolute ethanol) for 24 h and washed with absolute ethanol. Pt counter electrodes were prepared on the FTO glass using 5 mM H_2PtCl_6/2-propanol solution, followed by heating at 400°C for 30 min. The washed working electrode was assembled with the Pt-coated counter electrode into a sandwich-type cell and sealed with 60 μm Surlyn. Then I^-/I^{3-} electrolyte containing 0.60 M BMII, 0.1 M LiI, 0.05-M I_2, and 0.5 M *tert*-butylpyridine in acetonitrile was injected into the cell.

The photocurrent–voltage (I–V) characteristics of the assembled

DSSCs were evaluated using a 530 W xenon lamp (XIL model 05A50KS source units; AM 1.5 solar irradiance; intensity: 100 mW cm^{-2}). The incident photon-to-current efficiency (IPCE, PV Measurements, Inc.) was measured from 300 to 800 nm under short-circuit conditions. EIS measurement was performed under a light illumination of 100 mW cm^{-2} using a Zahner Electrik IM6 analyzer. The applied bias voltage and ac amplitude were set at the open circuit voltage of DSSCs and 10 mV between the FTO/Pt counter electrode and the FTO/TiO_2/dye working electrode, respectively. The frequency range was explored from 10 mHz to 1 Hz. The impedence spectra were analyzed using an equivalent circuit model.

2.2. β-$NaYF_4$:Yb^{3+}, Er^{3+} hexagonal nanoprisms for perovskite solar cells

2.2.1. Fabrication of β-$NaYF_4$:Yb^{3+}, Er^{3+} hexagonal nanoprisms

$NaYF_4$:Yb^{3+}, Er^{3+} hexagonal nanoprisms were synthesized using a modified hydrothermal process.[51] Typically, 7.8 mL of yttrium(III) nitrate hexahydrate (0.2 M, 99.8%, Sigma-Aldrich), 2 mL of ytterbium(III) nitrate pentahydrate (0.2 M, 99.9%, Sigma-Aldrich) and 0.2 mL of Erbium(III) nitrate pentahydrate (0.2 M, 99.9%, Sigma-

Aldrich) were added to 20 mL of aqueous sodium citrate solution (2 M, ≥99.9%, Sigma-Aldrich) and stirred for 1 h to form Ln^{3+}-citrate complex. Then, 40 mL of aqueous solution containing ammonium fluoride (2.4 M, ≥98.0%, Sigma-Aldrich) was introduced to the above solution and stirred for 1 h. pH of the mixing solution was adjusted to 3 by nitric acid. After additional stirring for 5 min, the mixture was transferred to a 100 mL Teflon-lined stainless steel autoclave and heated at 180°C for 2 h. White precipitates were collected by centrifugation, washed with water and ethanol, and then dried at 60°C in a vacuum oven.

2.2.2. Characterization of β-$NaYF_4$:Yb^{3+}, Er^{3+} hexagonal nanoprisms

The morphology of the $NaYF_4$:Yb^{3+}, Er^{3+} hexagonal nanoprisms, upconverting mesoporous layer and cross sectional view of perovskite solar cell was observed by Field-emission scanning electron microscopy (FE-SEM) a JEOL 6700. X-ray diffraction (XRD) was performed using a Bruker New D8 Advance with a Cu-Kα radiation source (λ: 1.5406 Å) at 40 kV and 300 mA (12 kW). The Upconversion photoluminescence (PL) spectrum of the $NaYF_4$:Yb^{3+},

Er^{3+} hexagonal nanoprisms was measured by a homemade spectrometer equipped with a 980 nm laser (SDL-980LM-500T, Shanghai Dream Lasers Technology), a monochromator (HoloSpec f/ 1.8i, Kaiser Optical Systems), and a charge-coupled device (CCD) camera (PIXIS 400BR, Princeton Instruments).

2.2.3. Application to perovskite solar cell

TiO_2 paste was prepared by adding ethyl cellulose, lauric acid, and terpineol to an ethanol solution of TiO_2 nanoparticles, followed by stirring and sonication. TiO_2 nanoparticles were synthesized using a two-step hydrothermal method reported previously.[101] Ethanol was removed using a rotary evaporator. The paste was then mixed using a 3-roll mill to create a homogeneous mixture. The nominal composition of TiO_2/terpineol/ethyl cellulose /lauric acid was 1.25/6/0.9/0.3. The $NaYF_4$:Yb^{3+}, Er^{3+} paste was prepared in the same manner as described above. Patterned FTO glass (8 Ω/sq, Filkington) was cleaned by sonication in distilled water, acetone, and 2-propanol for 60 min each. An ethanolic solution of colloidal TiO_2 nanoparticles and titanium diisopropoxide bis(acetylacetonate) (75 wt. % in isopropanol, Aldrich) was spin-coated on FTO glass at 5000 rpm for

30 s and heated at 150°C for 20 min to prepare the compact TiO_2 layer.[102] To prepare a $NaYF_4:Yb^{3+}$, Er^{3+} upconverting mesoporous layer, the TiO_2 paste was mixed with the $NaYF_4:Yb^{3+}$, Er^{3+} paste by a ratio of 1:3, 1:1 and 3:1 (25, 50 and 75 wt% $NaYF_4:Yb^{3+}$, Er^{3+} respectively). The mixed paste diluted in ethanol at a weight ratio of 1:5 were spin-coated on the compact TiO_2 layer at 3000 rpm for 30 s and annealed at 500°C for 30 min. The upconverting mesoporous flim was post-treated with aqueous $TiCl_4$ solution (20 mM, >98%, Aldrich) at 70°C for 20 min and sintered at 500°C for 30 min. To fabricate methylammonium lead iodide perovskite ($CH_3NH_3PbI_3$) film, perovskite precursor solution was prepared by mixing 461 mg of PbI_2 (99.9985%, Alpha Aesar), 159 mg of CH_3NH_3I and 78 μL of dimethyl sulfoxide (DMSO, 99.5%, Sigma-Aldrich) (molar ratio 1:1:1) in 770 μL of N, N-dimethylformamide (DMF, 99.8%, Sigma-Aldrich) at a room temperature for 1 h. CH_3NH_3I was synthesized by the method reported elsewhere using methylamine (40 wt% in water, Sigma-Aldrich) and hydriodic acid (57 wt% in water, Sigma-Aldrich).[101] The completely dissolved solution was spin-coated on the upconverting mesoporous layer at 3000 rpm for 90 s, and 500 μL of diethyl ether was dripped at 10 s onto the rotating substrate. The

precursor-coated film was heated on a hot plate at 65°C for 1 min and 100°C for 60 min. Then the Spiro-OMeTAD solution was spin-coated on the perovskite layer at 3500 rpm for 30 s. The Spiro-OMeTAD solution was prepared by mixing 72 mg of Spiro-MeOTAD (Lumtec), 28.8 μL of tert-butylpyridine and 17.5 μL of acetonitrile solution containing 520 mg/mL lithium bis(trifluoromethylsulfonyl)imide salt in 1 mL of chlorobenzene. Finally, a 70 nm thick Au top electrode was deposited by thermal evaporation. The active area of the fabricated device was 0.09 cm^2. The photocurrent–voltage (J–V) characteristics of the fabricated perovskite solar cells were evaluated using a 530 W xenon lamp (XIL model 05A50KS source units; AM 1.5 solar irradiance; intensity: 100 mW cm^{-2}). The incident photon-to-current efficiency (IPCE, PV Measurements, Inc.) was measured from 300 to 900 nm under short-circuit conditions. Electrochemical Impedance Spectroscopy (EIS) measurement was performed using a Zahner Electrik IM6 analyzer under a dark condition.

2.3. Size-controlled Ag@SiO_2 nanoplates for perovskite solar cells

2.3.1. Fabrication of size-controlled Ag@SiO_2 nanoplates

The Ag nanoprisms were synthesized using a seed-mediated

procedure with a few modifications. First, aqueous sodium citrate (22.5 mL, 2.5 mM), aqueous poly(sodium styrene sulfonate) (PSSS, 2.5 mg), and aqueous $NaBH_4$ (1.5 mL, 10 mM) , freshly prepared and cooled at 0 °C) were mixed together successively followed by addition of aqueous $AgNO_3$ (15 mL, 0.5 mM) at a rate of 2 mL/min while the mixture was being continuously stirred. Then the yellow solution of Ag seeds was obtained. Second, 25 mL of ultrapure water was mixed with aqueous L-ascorbic acid (0.375 mL, 10 mM) and various amounts of seed solution (from 0.05 mL to 1 mL), followed by the mixture being dropped into aqueous $AgNO_3$ (15 mL, 0.5 mM) at a rate of 1 mL/min. After that, aqueous trisodium citrate (2 mL, 25 mM) was injected to stabilize the nanoprisms. Under magnetic stirring, the color of the solution changed gradually during the dropping of the $AgNO_3$ solution. The product was directly used for Ag@SiO_2 core–shell nanoplates without further purification.

Fabricated Ag nanoprisms were functionalized by the addition of a 5.0 mM ethanolic solution of 16-mercaptohexadecanoic acid (MHA); enough solution was added to bring the final thiol concentration to 60 μM. After stirring for 10 min, the functionalized nanoprisms were collected by centrifugation at 15000 rpm for 1.5 h, and were

redispersed in ethanolic tetraethoxysilane. The entire synthesis procedure was carried in presence of 0.6 M dimethylamine (DMA) using 20% aqueous DMA and stirred for 12 h.

2.3.2. Characterization of size-controlled Ag@SiO_2 nanoplates

The morphology of size-controlled Ag and Ag@SiO_2 nanoplates was observed by energy-filtering transmission electron microscopy (EF-TEM, Carl Zeiss LIBRA 120). Field-emission scanning electron microscopy (FE-SEM) was obtained with a JEOL 6700. A Lambda 35 (Perkin-Elmer) UV-Vis spectrometer was used for investigating the extinction of Ag and Ag@SiO_2 nanoplates and absorption spectrum of perovskite film.

2.3.1. Application to perovskite solar cells

TiO_2 paste was prepared by adding ethyl cellulose, lauric acid, and terpineol to an ethanol solution of TiO_2 nanoparticles, followed by stirring and sonication. TiO_2 nanoparticles were synthesized using a two-step hydrothermal method reported previously.[101] Ethanol was removed using a rotary evaporator. The paste was then mixed using a 3-roll mill to create a homogeneous mixture. The nominal

composition of TiO_2/terpineol/ethyl cellulose /lauric acid was 1.25/6/0.9/0.3. Patterned FTO glass (8 Ω/sq, Filkington) was cleaned by sonication in distilled water, acetone, and 2-propanol for 60 min each. An ethanolic solution of colloidal TiO_2 nanoparticles and titanium diisopropoxide bis(acetylacetonate) (75 wt. % in isopropanol, Aldrich) was spin-coated on FTO glass at 5000 rpm for 30 s and heated at 150°C for 20 min to prepare the compact TiO_2 layer.[102] To incorporate Ag@SiO_2 nanoplates into mesoporous layer, the TiO_2 paste was mixed with the Ag@SiO_2 nanoplates by ratios ranging from 0.2wt% to 1wt% (with respect to TiO_2 nanoparticles). The mixed paste diluted in ethanol at a weight ratio of 1:5 were spin-coated on the compact TiO_2 layer at 3000 rpm for 30 s and annealed at 500°C for 30 min. The mesoporous flim was post-treated with aqueous $TiCl_4$ solution (20 mM, >98%, Aldrich) at 70°C for 20 min and sintered at 500°C for 30 min. To fabricate methylammonium lead iodide perovskite ($CH_3NH_3PbI_3$) film, perovskite precursor solution was prepared by mixing 461 mg of PbI_2 (99.9985%, Alpha Aesar), 159 mg of CH_3NH_3I and 78 μL of dimethyl sulfoxide (DMSO, 99.5%, Sigma-Aldrich) (molar ratio 1:1:1) in 770 μL of N, N-dimethylformamide (DMF, 99.8%, Sigma-Aldrich) at a room temperature for 1 h.

CH_3NH_3I was synthesized by the method reported elsewhere using methylamine (40 wt% in water, Sigma-Aldrich) and hydriodic acid (57 wt% in water, Sigma-Aldrich).[101] The completely dissolved solution was spin-coated on the mesoporous layer at 3000 rpm for 90 s, and 500 μL of diethyl ether was dripped at 10 s onto the rotating substrate. The precursor-coated film was heated on a hot plate at 65°C for 1 min and 100°C for 60 min. Then the Spiro-OMeTAD solution was spin-coated on the perovskite layer at 3500 rpm for 30 s. The Spiro-OMeTAD solution was prepared by mixing 72 mg of Spiro-MeOTAD (Lumtec), 28.8 μL of tert-butylpyridine and 17.5 μL of acetonitrile solution containing 520 mg/mL lithium bis(trifluoromethylsulfonyl)imide salt in 1 mL of chlorobenzene. Finally, a 70 nm thick Au top electrode was deposited by thermal evaporation. The active area of the fabricated device was 0.09 cm^2. The photocurrent–voltage (J–V) characteristics of the fabricated perovskite solar cells were evaluated using a 530 W xenon lamp (XIL model 05A50KS source units; AM 1.5 solar irradiance; intensity: 100 mW cm^{-2}). The incident photon-to-current efficiency (IPCE, PV Measurements, Inc.) was measured from 300 to 900 nm under short-circuit conditions.

3. RESULTS AND DISCUSSION

3.1. $CeO_2:Eu^{3+}$ nano-octahedra for dye-sensitized solar cells

3.1.1. Fabrication of $CeO_2:Eu^{3+}$ nano-octahedra

$CeO_2:Eu^{3+}$ nano-octahedra were synthesized by a simple hydrothermal process with slight modification. $Ce(NO_3)_3$ was used as the precursor to CeO_2 nano-octahedra; $Eu(NO_3)_3$ was used as the Eu^{3+} dopant. Na_3PO_4, a mineralizer, played a prominent role in the development of the octahedral morphology of the $CeO_2:Eu^{3+}$ nano-octahedra.[103] $Ce(NO_3)_3$ and $Eu(NO_3)_3$ were dissolved in distilled water. Na_3PO_4 was then added to the aqueous solution to generate OH^- ions *via* hydrolysis. Ce^{3+} ions were further oxidized by O_2 in the aqueous system. The hydrated Ce^{4+} and Eu^{3+} ions formed complexes with the H_2O molecules or OH^- ions, taking the form of $Ce(H_2O)_x(OH^-)_y^{(4-y)+}$ and $Eu(H_2O)_x(OH^-)_y^{(3-y)+}$. In the hydrothermal process, polar H_2O molecules in the solution took protons away from the coordinated hydroxides in Ce^{4+} or Eu^{3+} complexes, resulting in the formation of $CeO_2:Eu^{3+}$ nano-octahedra.[104] The Eu^{3+} concentration in $CeO_2:Eu^{3+}$ nano-octahedra was adjusted by controlling the amount of $Eu(NO_3)_3$. The amount of Eu^{3+} in $CeO_2:Eu^{3+}$ nano-octahedra was confirmed by EDS analysis (**Table 1**), ranging from 0.1 to 2 mol%.

The morphology of the synthesized $CeO_2:Eu^{3+}$ nano-octahedra was investigated *via* TEM and SEM observation. **Figure 6** shows TEM images of $CeO_2:Eu^{3+}$ nano-octahedra. **Figure 7** shows FE-SEM images of $CeO_2:Eu^{3+}$ nano-octahedra with 1 mol% Eu^{3+}. The fabricated $CeO_2:Eu^{3+}$ nano-octahedra had an octahedral structure with well-defined corners, edges, and mirror-like facets, corresponding to the {111} plane of CeO_2 (Figure 1a–c). The size of the $CeO_2:Eu^{3+}$ nano-octahedra ranged from 300–400 nm. The HR-TEM image in **Figure 8** revealed that the $CeO_2:Eu^{3+}$ nano-octahedra had well-developed two-dimensional (2D) lattice planes and good crystallinity. The *d*-spacing of 0.32 nm was well matched with the {111} plane of face-centered CeO_2. The SAED pattern of the $CeO_2:Eu^{3+}$ nano-octahedra corresponded to the $(\bar{1}11)$, (002), and $(1\bar{1}1)$ planes of single-crystalline CeO_2 (**Figure 9**); thus, the structure of the $CeO_2:Eu^{3+}$ nano-octahedra was assigned to face-centered CeO_2, consistent with HR-TEM analysis. Compared with pristine CeO_2 nano-octahedra, the Eu^{3+} ions did not influence the morphology of the $CeO_2:Eu^{3+}$ nano-octahedra with increasing Eu^{3+} content (**Figure 10**).

Table 1. Energy disperse X-ray spectroscopy (EDS) analysis of the CeO_2:Eu^{3+} nano-octahedra.

Sample	Atomic ratio (%)		
	Ce	Eu	O
CeO_2:0.1% Eu^{3+}	26.13	0.12	73.75
CeO_2:0.2% Eu^{3+}	26.75	0.24	73.01
CeO_2:0.5% Eu^{3+}	25.56	0.51	73.93
CeO_2:1% Eu^{3+}	24.54	1.17	74.29
CeO_2:2% Eu^{3+}	23.63	2.06	74.31

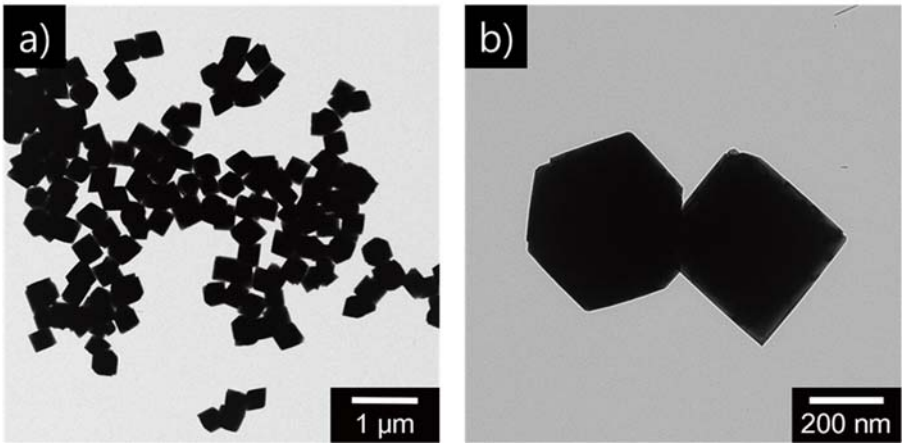

Figure 6. a, b) Transmission electron microscope (TEM) images of CeO_2:Eu^{3+} nano-octahedra (1 mol% Eu^{3+}).

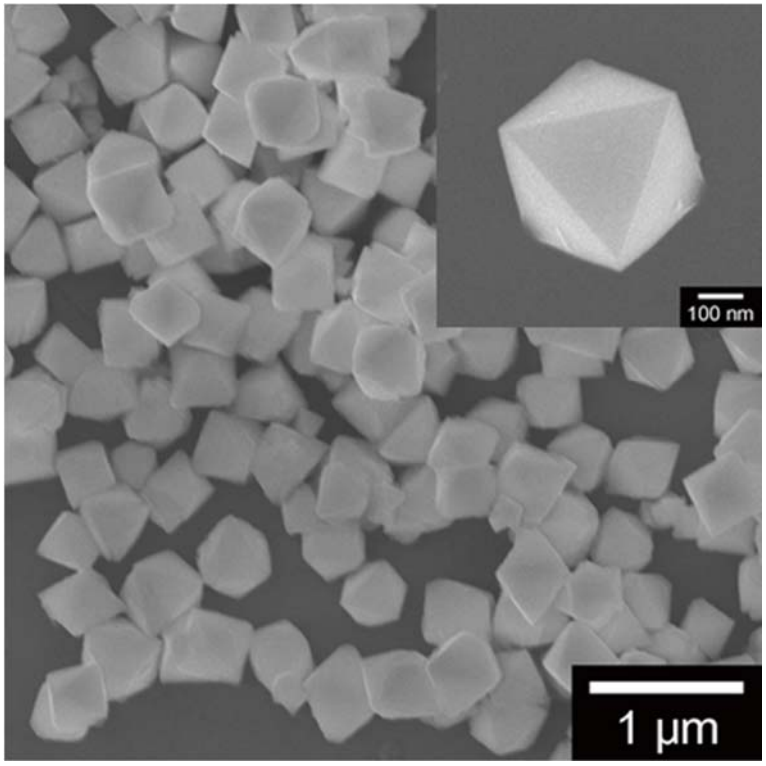

Figure 7. Scanning electron microscope (SEM) images of $CeO_2:Eu^{3+}$ nano-octahedra (1 mol% Eu^{3+}).

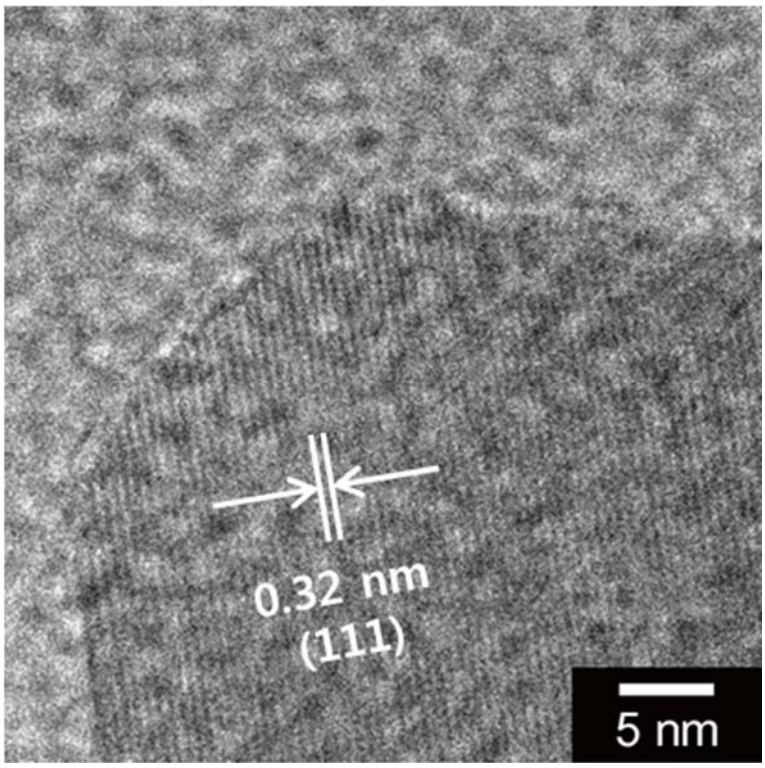

Figure 8. The HR-TEM image of CeO_2:Eu^{3+} nano-octahedra (1 mol% Eu^{3+}).

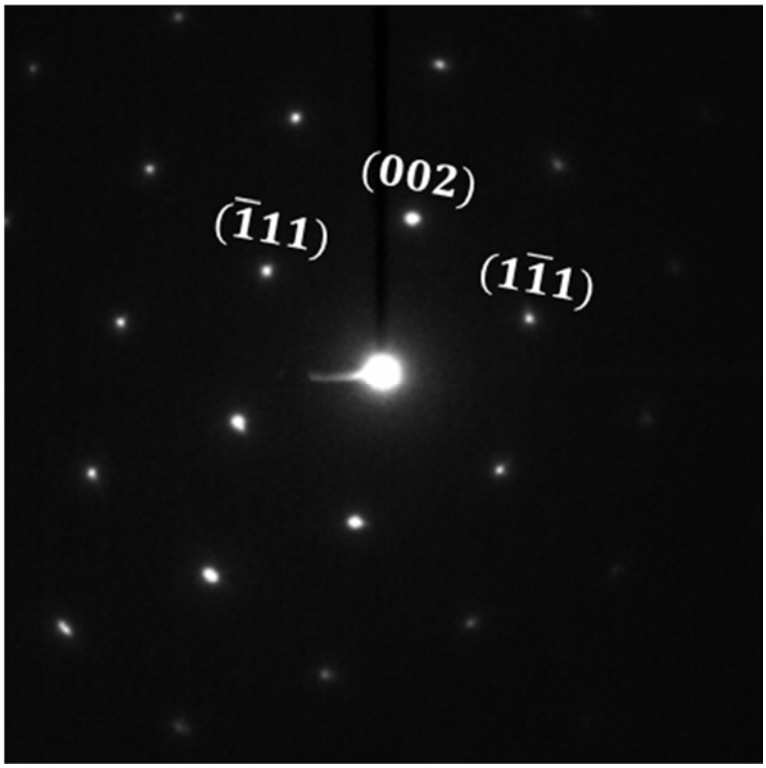

Figure 9. The selected area electron diffraction (SAED) pattern of CeO_2:Eu^{3+} nano-octahedra (1 mol% Eu^{3+}).

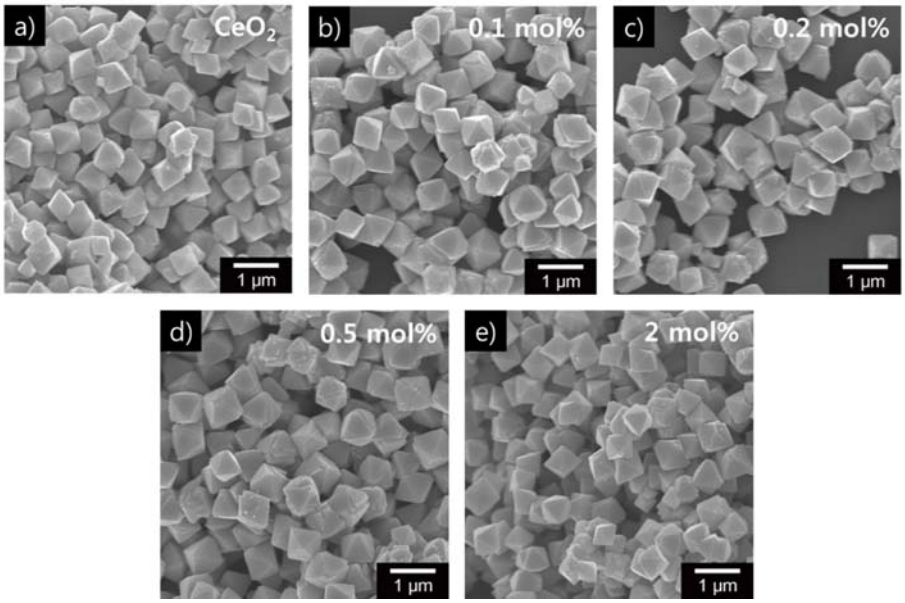

Figure 10. SEM images of CeO_2:Eu^{3+} nano-octahedra with various Eu^{3+} concentrations: a) pristine CeO_2 nano-octahedra, b) 0.1 mol%, c) 0.2 mol%, d) 0.5 mol%, and e) 2 mol%.

3.1.2. Characterization of $CeO_2:Eu^{3+}$ nano-octahedra

The crystallinity of the $CeO_2:Eu^{3+}$ nano-octahedra was confirmed by the XRD patterns (**Figure 11**). The diffraction peaks of the CeO_2 and $CeO_2:Eu^{3+}$ nano-octahedra were identical and corresponded exactly to the (111), (200), (220), (311), (222), (400), (331), and (420) planes of pure cubic fluorite CeO_2. In addition, the peaks of Eu, Eu_2O_3, and $Eu(OH)_3$ were not observed in the $CeO_2:Eu^{3+}$ nano-octahedra. Considering the SAED and XRD patterns, these results suggest that the Eu^{3+} ions entered the CeO_2 lattices during the hydrothermal process and substituted for the Ce^{4+} ions without changing the cubic fluorite CeO_2 structure.

XPS analysis was carried out to identify the presence of Eu^{3+} ions in $CeO_2:Eu^{3+}$ nano-octahedra (**Figure 12**). The peaks at 916.9 and 898.5 eV were assigned to the Ce^{4+} $3d_{3/2}$ and Ce^{4+} $3d_{5/2}$ contributions. The peaks centered at 901.2 and 882.6 eV corresponded to the binding energy of Ce^{3+} $3d_{3/2}$ and Ce^{3+} $3d_{5/2}$, which indicates that a small amount of Ce^{3+} was present on the CeO_2 surface. The existence of a small amount of Ce^{3+} at the surface of CeO_2 is well known; moreover, the fraction of Ce^{3+} ions increases with decreasing particle size.[105] The peaks at 1164.2 and 1134.5 eV corresponded to the binding

energy of Eu^{3+} $3d_{3/2}$ and Eu^{3+} $3d_{5/2}$, which indicated that europium ions in the CeO_2 lattices existed in the form of trivalent ions (Eu^{3+}). These results suggest that the CeO_2:Eu^{3+} nano-octahedra possess europium ions in the Eu^{3+} form, as well as a small portion of Ce^{3+} ions.

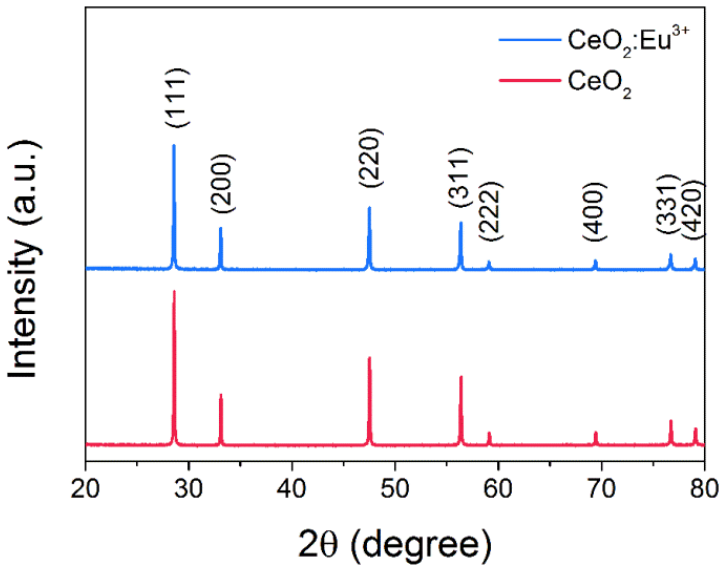

Figure 11. X-ray diffraction (XRD) patterns of CeO_2 and $CeO_2:Eu^{3+}$ nano-octahedra (1 mol% Eu^{3+}).

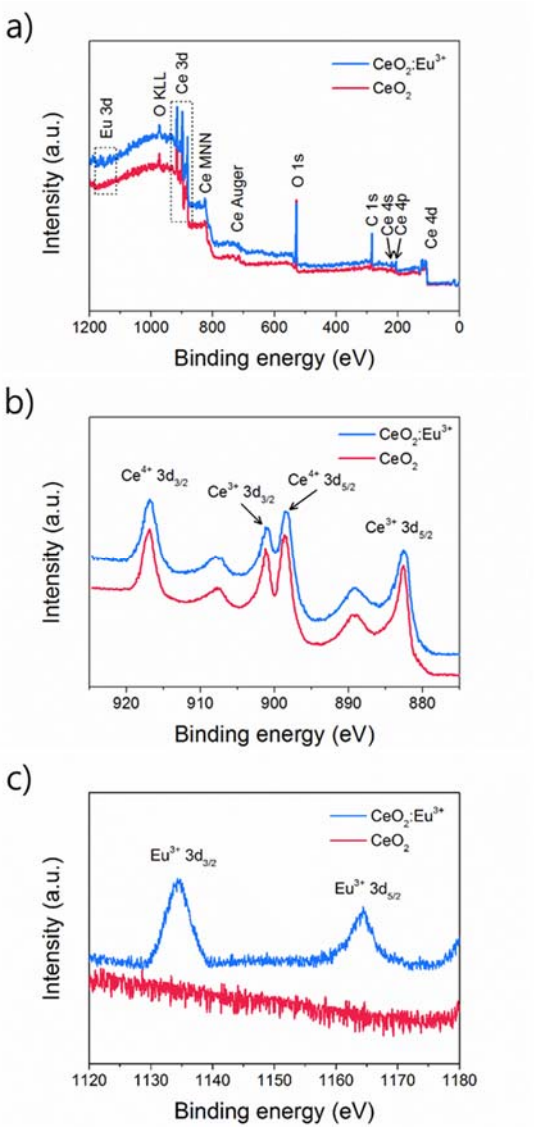

Figure 12. X-ray photoelectron spectroscopy (XPS) analysis showing b) a full scan, c) Ce 3d, and d) the Eu 3d regions of $CeO_2:Eu^{3+}$ nano-octahedra.

To investigate the light-scattering ability of $CeO_2:Eu^{3+}$ nano-octahedra, UV-Vis DRS was performed over the wavelength range of 300–800 nm (**Figure 13a**). The thicknesses of the pristine P25 film, CeO_2-incorporated P25 film, and $CeO_2:Eu^{3+}$-incorporated P25 film were adjusted to 10 μm. The diffuse reflectance of the CeO_2 and $CeO_2:Eu^{3+}$ films was > 60% in the range of 400–800 nm (**Figure 13a**), much higher than that of the pure P25 film. This improvement in the diffuse reflectance was attributed to effective light scattering by the large size and mirror-like facets of the octahedral CeO_2 and $CeO_2:Eu^{3+}$ nano-octahedra. These mirror-like facets increased the optical pathlength of the incident light by reflecting the incident light directly back to the TiO_2 films, resulting in enhancement of the photocurrent density in the DSSC.[106] The band gap energy (E_g) of the P25 film, P25+CeO_2 film and the P25+$CeO_2:Eu^{3+}$ film can be determined by Kubelka-Munk transformation of diffuse reflectance data. **Figure 13b** shows the Kubelka-Munk plot for the P25 film, P25+CeO_2 (20 wt%) film and the P25+$CeO_2:Eu^{3+}$ film (20 wt%, 1 mol% Eu^{3+}). From the extrapolation of the linear part of Kubelka-Munk plot, E_g for P25 film, P25+CeO_2 film and the P25+$CeO_2:Eu^{3+}$ film are determined to be 3.11, 2.98 and 2.94 eV respectively. Therefore, E_g of the P25+$CeO_2:Eu^{3+}$

film are narrower than those of P25+CeO_2 film and the P25+CeO_2:Eu^{3+} film, which is indicated a better response in the visible region of the solar spectrum.

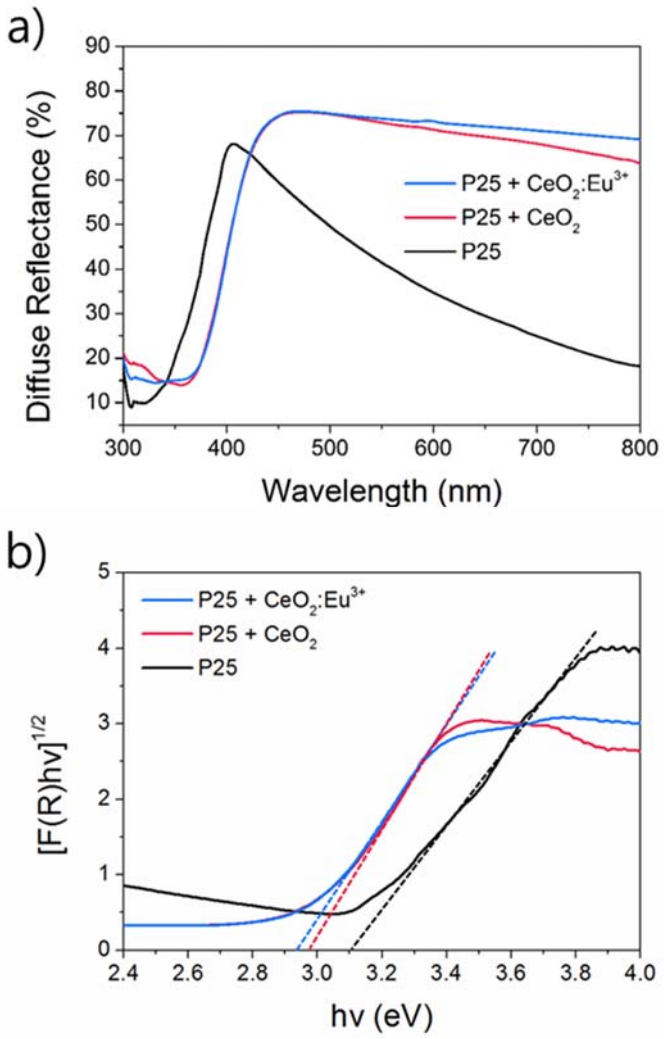

Figure 13. a) UV-Vis diffuse reflectance spectra (DRS) and b) transformed Kubelka-Munk spectra of a pristine P25 film, a P25+CeO_2 (20 wt%) film, and a P25+CeO_2:Eu^{3+} film (20 wt%, 1 mol% Eu^{3+}).

The downconversion PL properties were investigated by measuring the PL spectra of $CeO_2:Eu^{3+}$ nano-octahedra. **Figure 14a** shows the excitation spectra of $CeO_2:Eu^{3+}$ nano-octahedra with increasing Eu^{3+} concentration (0.1–2 mol% Eu^{3+}). All excitation spectra of the $CeO_2:Eu^{3+}$ nano-octahedra have broad bands with a maximum at 330 nm, which is attributed to the excitation of the host CeO_2 nano-octahedra. The intensity of the excitation bands increased with increasing concentration of Eu^{3+} dopant and reached a maximum at 1 mol% Eu^{3+}. With a further increase in the Eu^{3+} concentration, the excitation intensity decreased due to concentration quenching of Eu^{3+} emission caused by cross-relaxation and energy migration among Eu^{3+} ions.[107]

Figure 14b shows the PL emission spectra of $CeO_2:Eu^{3+}$ nano-octahedra excited at 330 nm. The typical Eu^{3+} emission peaks at 570, 590, 610, 631, 650, and 672 nm were observed in all $CeO_2:Eu^{3+}$ nanocrystals; these peaks were assigned to the $^5D_0 \rightarrow {}^7F_J$ (J = 0-4) transitions of Eu^{3+} ions, as follows: $^5D_0 \rightarrow {}^7F_0$ (570 nm), $^5D_0 \rightarrow {}^7F_1$ (590 nm), $^5D_0 \rightarrow {}^7F_2$ (610 and 631 nm), $^5D_0 \rightarrow {}^7F_3$ (650 nm), and $^5D_0 \rightarrow {}^7F_4$ (672 nm). It is known that the $^5D_0 \rightarrow {}^7F_1$ transition is a magnetic dipole transition that is insensitive to the crystal field strength around

the Eu^{3+} ions, while the $^5D_0 \rightarrow {}^7F_2$ transition is hypersensitive to the local symmetry around the Eu^{3+} ions due to the electric dipole transition of $^5D_0 \rightarrow {}^7F_2$.[108] For this reason, when the Eu^{3+} ions are located in the CeO_2 lattice with an inversion symmetry, the $^5D_0 \rightarrow {}^7F_1$ transition dominates the emission spectrum. On the other hand, when the Eu^{3+} ions are positioned at sites without inversion symmetry, the $^5D_0 \rightarrow {}^7F_2$ transition dominates the emission spectrum and its intensity increases with increasing lattice distortion around the Eu^{3+} ions.[109] In Figure 4b, the $^5D_0 \rightarrow {}^7F_1$ transition at 590 nm is a dominant peak in the emission spectra of CeO_2:Eu^{3+} nano-octahedra. This result suggests that the Eu^{3+} ions are located in CeO_2 lattices that possess inversion symmetry and that the structure of the CeO_2 lattices is maintained with increasing Eu^{3+} concentration in CeO_2:Eu^{3+} nano-octahedra. The intensity of the $^5D_0 \rightarrow {}^7F_1$ transition increased gradually up to 1 mol% Eu^{3+}, followed by a decrease in the luminescence intensity with further increase in the Eu^{3+} concentration (*i.e.*, concentration quenching). Together, these findings indicate that the host CeO_2 absorbed the UV light and transferred energy to the Eu^{3+} ions in CeO_2 nonradiatively. The Eu^{3+} ions then re-emitted the transferred energy as visible light *via* downconversion PL corresponding to the $^5D_0 \rightarrow {}^7F_J$ transition.

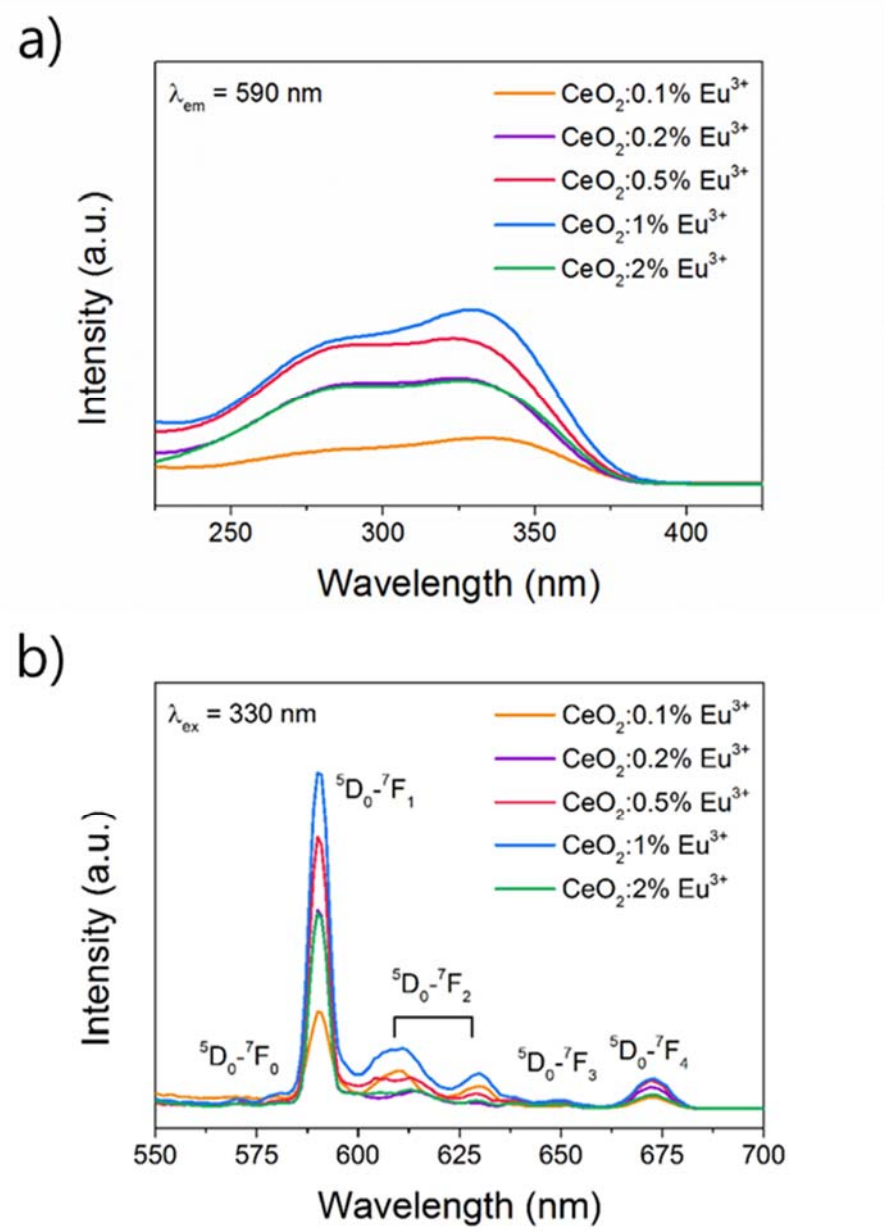

Figure 14. a) Excitation and b) emission spectra of the CeO_2:Eu^{3+} nanocrystals for various Eu^{3+} concentrations (0.1–2 mol%).

To confirm the possibility of using this PL effect in DSSCs, the emission spectra for $CeO_2:Eu^{3+}$ nano-octahedra were investigated before and after the addition of the D719 dye. **Figure 15** shows the emission spectra of bare $CeO_2:Eu^{3+}$ nano-octahedra and $CeO_2:Eu^{3+}$ nano-octahedra with N719 dye. In contrast to that of bare $CeO_2:Eu^{3+}$ nano-octahedra, the emission spectrum intensity of $CeO_2:Eu^{3+}$ nano-octahedra with N719 dye decreased significantly. This decrease in the emission intensity was attributed to emission quenching of the emitted PL due to absorption by the N719 dye surrounding the $CeO_2:Eu^{3+}$ nano-octahedra. Thus, UV light can be utilized in DSSCs to improve photocurrent and power conversion performance via N719 absorption of the downconversion PL of $CeO_2:Eu^{3+}$ nano-octahedra.

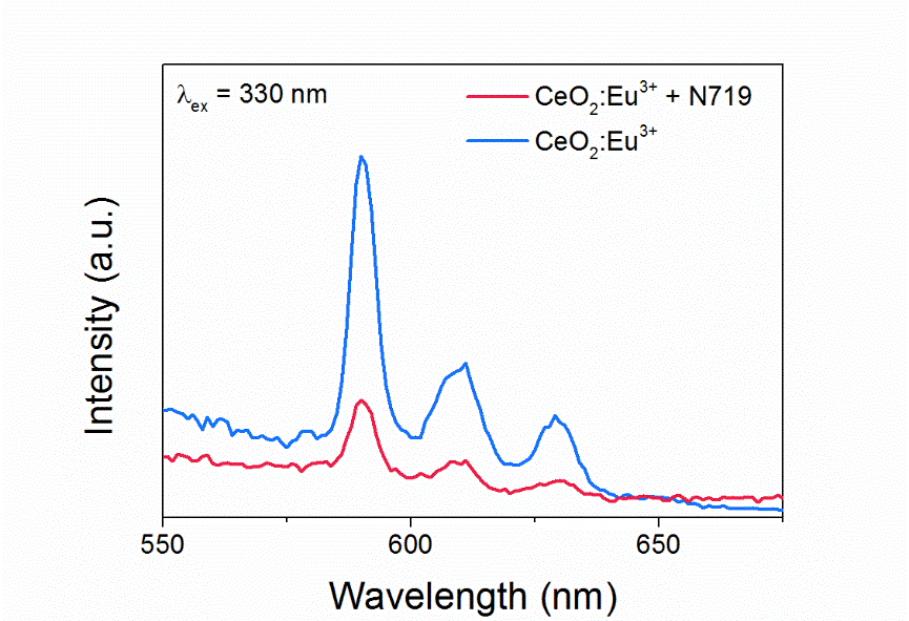

Figure 15. Emission spectra of $CeO_2:Eu^{3+}$ nano-octahedra (1 mol% Eu^{3+}) with N719 dye.

3.1.3. Application to dye-sensitized solar cells

Bilayer DSSC devices, with a CeO_2 or CeO_2:Eu^{3+} layer on a P25 control film, were assembled to evaluate the light-scattering and downconversion effect on photovoltaic performance (**Figure 16**). P25-CeO_2 and P25-CeO_2:Eu^{3+} photoanodes were prepared by successive screen-printing with the mixed P25-CeO_2:Eu^{3+} paste onto P25 reference photoanodes. The surface morphology and cross-section of the assembled DSSC photoanodes are given in **Figure 17**. The photocurrent density–voltage (*J-V*) curves of the P25, P25-CeO_2, and P25-CeO_2:Eu^{3+} photoanodes are shown in **Figure 18a**, and their photovoltaic properties are summarized in **Table 2**. The DSSC with the P25 control photoanode exhibited a short-circuit current density (J_{sc}) of 14.04 mA cm^{-2} and a PCE (η) of 7.33%. With the CeO_2 layer added to the P25 photoanode, J_{sc} and η increased to 14.33 mA cm^{-2} and 7.92%, leading to an 8.08% enhancement in efficiency compared with the P25 reference cell. This enhancement was attributed to the increase in the optical pathlength of light resulting from the excellent light-scattering effect of CeO_2 nano-octahedra. The effects of Eu^{3+} concentration in CeO_2:Eu^{3+} nano-octahedra on the efficiency are shown in **Figure 18b**, and the photovoltaic properties are listed in

Table 3. The DSSCs with a CeO_2:Eu^{3+} layer exhibited a slightly enhanced J_{sc} and η, compared with the DSSC with a CeO_2 layer (**Table 3**). With increasing Eu^{3+} concentration in the CeO_2:Eu^{3+} nano-octahedra, J_{sc} and η increased up to 1 mol%, followed by a decrease in J_{sc} and η with further increase in the Eu^{3+} concentration (**Figure 18b**). The best performance was obtained using a P25-CeO_2:Eu^{3+} photoanode with a Eu^{3+} concentration of 1 mol%, demonstrating J_{sc} and η values of 15.26 mA cm^{-2} and 8.36%, respectively. These results corresponded to a 5.49% enhancement in performance, compared with that of the P25-CeO_2 photoanode. This remarkable enhancement in J_{sc} and η was attributed to the downconversion luminescence properties of CeO_2:Eu^{3+} nano-octahedra from UV to visible light, which can be absorbed and utilized by the N719 dye. However, when the Eu^{3+} concentration in CeO_2:Eu^{3+} nano-octahedra exceeded 1 mol%, a decrease in J_{sc} was observed. This result may be associated with a decrease in the downconversion luminescence intensity by concentration quenching. The effect of CeO_2:Eu^{3+} layer thickness on the efficiency are shown in **Figure 19** and their photovoltaic performances are summarized in **Table 4**. Both J_{sc} and V_{oc} decreased with increasing the thickness of CeO_2:Eu^{3+} layer. The thick film has

larger surface area compared with thin film and provides the additional charge recombination sites.[110] In addition, CeO_2 owns intrinsic oxygen vacancies, which can result in electron-hole recombination.[111] When Eu^{3+} concentration increases gradually, the effects of CeO_2:Eu^{3+} nano-octahedra also increase. This increased defects may trap photogenerated electrons and cause the recombination of electrons and holes, thus reducing PCE.

Figure 20 shows IPCE spectra of the P25, P25-CeO_2, and P25-CeO_2:Eu^{3+} photoanodes. With introducing CeO_2 scattering layer, the IPCE value over the entire region of 400-800 nm was considerably enhanced by excellent light-scattering effect of CeO_2 nano-octahedra. The DSSCs with a CeO_2:Eu^{3+} layer exhibits a maximum IPCE value of 64.5 % at 530 nm due to downconversion PL of CeO_2:Eu^{3+} nano-octahedra. This result is in good agreement with the photovoltaic performance as showed in **Figure 18a**.

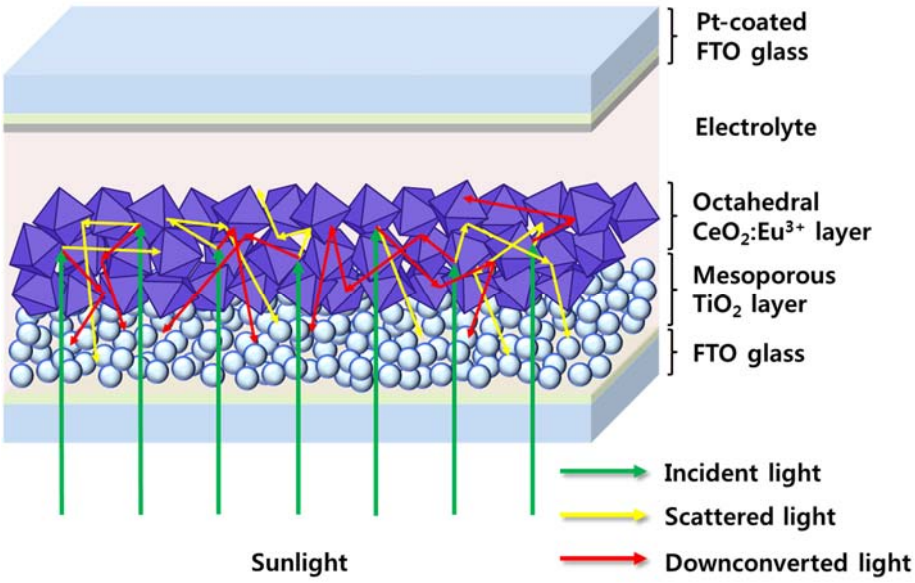

Figure 16. Schematic configuration of the bilayer DSSC device with $CeO_2:Eu^{3+}$ nano-octahedra for light scattering and downconversion.

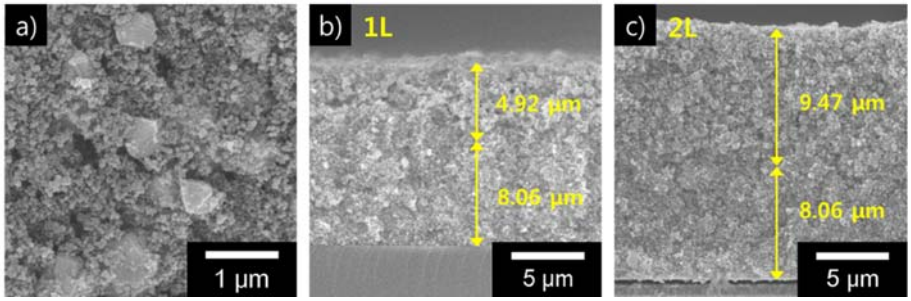

Figure 17. SEM images of a) surface morphology and cross-sectional structure of P25-CeO_2:Eu^{3+} photoanode with b) 1 layer and c) 2 layers.

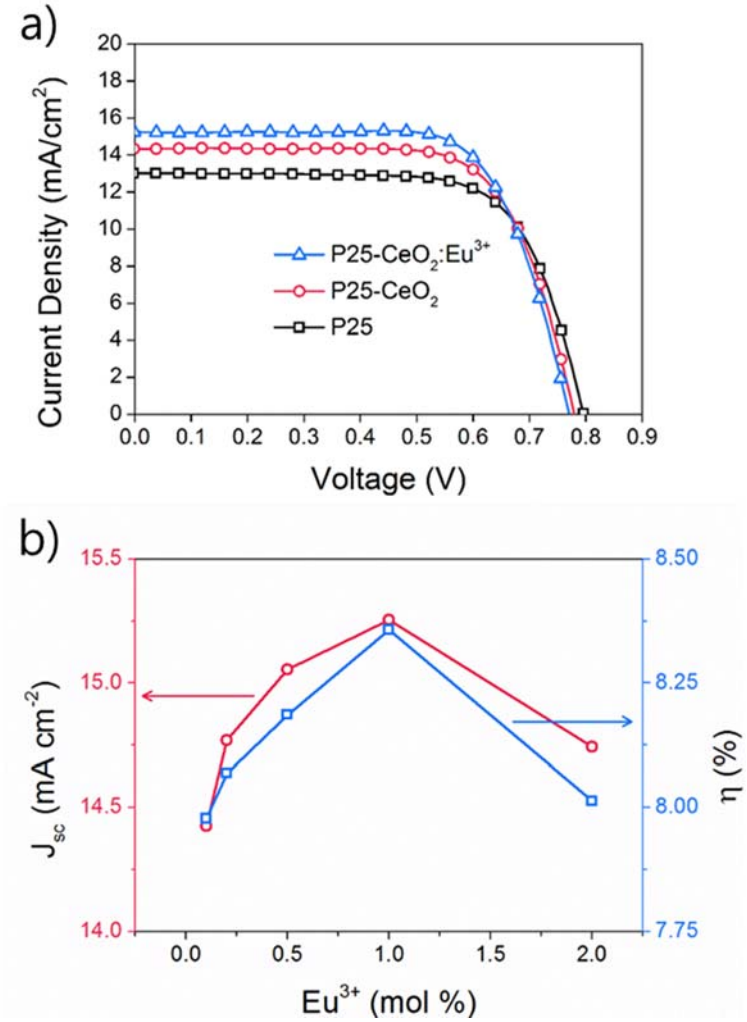

Figure 18. a) Photocurrent density–voltage characteristics (*J–V* curves) of the DSSCs using P25+CeO_2 (20 wt%) film, and a P25+CeO_2:Eu^{3+} film (20 wt%, 1 mol% Eu^{3+}) and b) the dependences of J_{sc} and η on the Eu^{3+} concentration of 0.1–2 mol %.

Table 2. Summary of the photovoltaic properties of dye-sensitized solar cells (DSSCs) with photoanodes containing CeO_2:Eu^{3+} nano-octahedra (1 mol% Eu^{3+}). Measurements were performed under AM 1.5G sunlight intensity of 100 W cm^{-2}.

Sample[a]	Thickness (μm)	J_{sc}[b] (mA cm^{-2})	V_{oc}[c] (V)	FF[d]	η[e] (%)	R_{ct} (Ω)
P25	8.06	13.040	0.796	0.706	7.330	2.8
P25-CeO_2	13.08	14.332	0.780	0.709	7.922	3.2
P25-CeO_2:Eu^{3+}	12.98	15.255	0.771	0.711	8.357	3.7

[a] Active area of the assembled DSSC samples is 0.16 cm^2; [b] short-circuit current; [c] open-circuit voltage; [d] fill factor; and [e] PCE.

Table 3. Summary of the photovoltaic properties of DSSCs with photoanodes containing CeO_2:Eu^{3+} nano-octahedra (0.1–2 mol% Eu^{3+}).

Sample	J_{sc} (mA cm^{-2})	V_{oc} (V)	FF	η (%)
CeO_2:0.1% Eu^{3+}	14.425	0.780	0.710	7.978
CeO_2:0.2% Eu^{3+}	14.771	0.771	0.709	8.069
CeO_2:0.5% Eu^{3+}	15.054	0.775	0.702	8.186
CeO_2:1% Eu^{3+}	15.255	0.771	0.711	8.357
CeO_2:2% Eu^{3+}	14.743	0.776	0.700	8.013

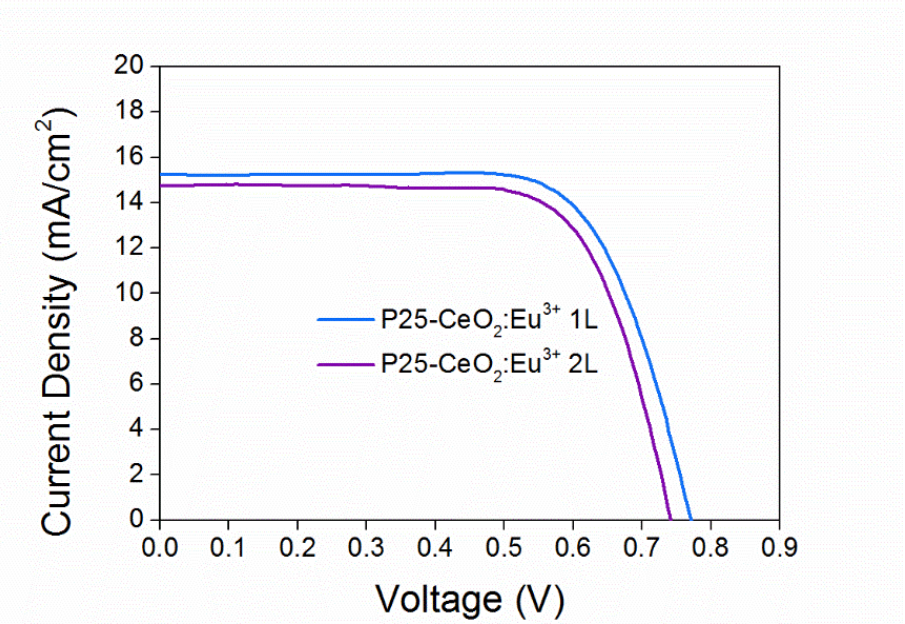

Figure 19. Photocurrent density–voltage characteristics (*J–V* curves) of downconversion-enhanced DSSCs with increasing $CeO_2:Eu^{3+}$ layer thickness.

Table 4. Summary of the photovoltaic properties of dye-sensitized solar cells (DSSCs) with different CeO_2:Eu^{3+} layer thicknesses (1 mol% Eu^{3+}).

Sample	Thickness (μm)	J_{sc} (mA cm^{-2})	V_{oc} (V)	*FF*	η (%)
P25-CeO_2:Eu^{3+} 1L	12.98	15.255	0.771	0.711	8.357
P25-CeO_2:Eu^{3+} 2L	17.53	14.791	0.743	0.714	7.839

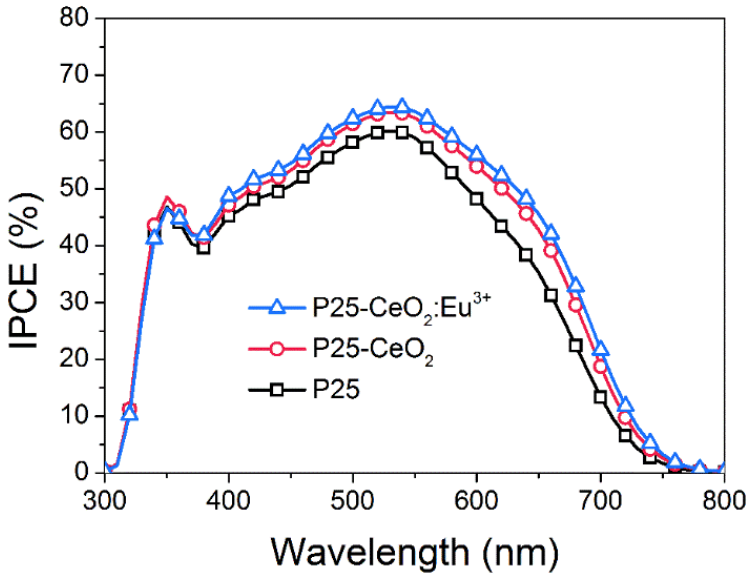

Figure 20. Incident photon to converted electron (IPCE) spectra o f the DSSCs using P25+CeO_2 (20 wt%) film, and a P25+CeO_2:Eu^{3+} film (20 wt%, 1 mol% Eu^{3+}).

To investigate the charge transfer in assembled DSSCs, EIS measurement was performed under a light intensity of 100 W cm^{-2}. **Figure 21** shows the Nyquist plots of DSSCs with the P25, P25-CeO_2, and P25-CeO_2:Eu^{3+} photoanodes. The small semicircle at higher frequency range (kHz range) corresponds to the charge transfer at the interfaces of the electrolyte/Pt counter electrode. The large semicircle in the mid-frequency region (1-100 Hz) is related to the transport of photoinduced electron at the TiO_2/dye/electrolyte.[112] The resistance values of assembled DSSCs at the TiO_2/dye/electrolyte interface (R_{ct}) are summarized in **Table 2**. As shown in **Figure 21**, The R_{ct} values of P25-CeO_2, and P25-CeO_2:Eu^{3+} DSSCs are higher than that of P25 reference cell, implying that inefficient charge transfer occurs in CeO_2 and CeO_2:Eu^{3+} layer. The higher R_{ct} can lead to lower charge transfer, which causes the charge recombination of photoinduced electrons. Considering these results, CeO_2:Eu^{3+} nano-octahedra can enhance the PCE by remarkable light-scattering and downconversion PL properties. However, the intrinsic defects of CeO_2:Eu^{3+} nano-octahedra are not beneficial for the electron transfer, which reduce photocurrent.

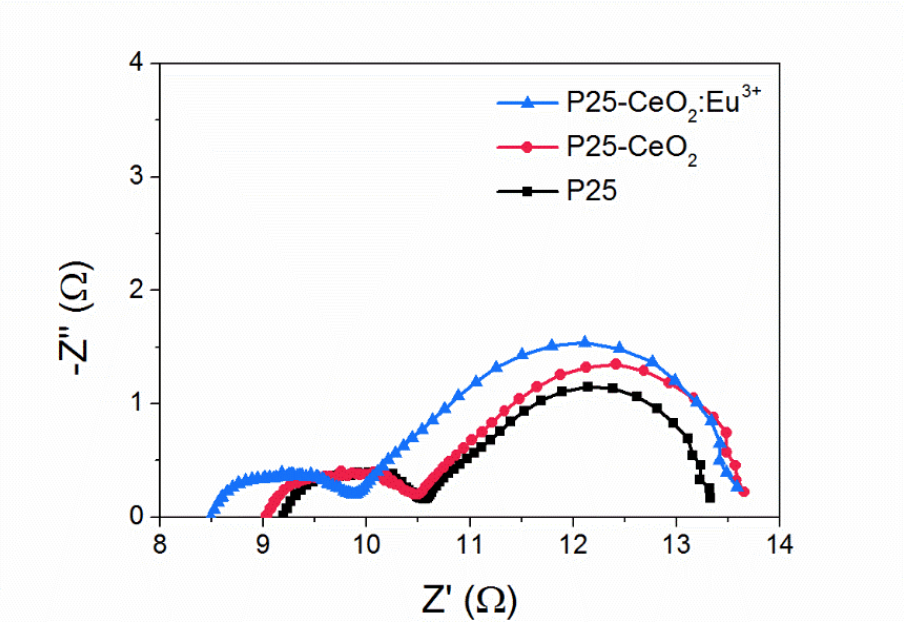

Figure 21. Nyquist plot of downconversion-enhanced DSSCs. Electrochemical impedance spectroscopy (EIS) measurement was performed under 100 mW cm^{-2}.

3.2 β-$NaYF_4$:Yb^{3+}, Er^{3+} hexagonal nanoprisms for perovskite solar cells

3.2.1 Fabrication of β-$NaYF_4$:Yb^{3+}, Er^{3+} hexagonal nanoprisms

$NaYF_4$:Yb^{3+}, Er^{3+} hexagonal nanoprisms were fabricated *via* a simple hydrothermal process using an aqueous solution containing trivalent lanthanide ions (Y^{3+}:Yb^{3+}:Er^{3+} = 78:20:2), sodium citrate, and ammonium fluoride.[55, 113] The morphology of the $NaYF_4$:Yb^{3+}, Er^{3+} nanoprisms was investigated by scanning electron microscopy (SEM). **Figure 22** shows a representative SEM image of the $NaYF_4$:Yb^{3+}, Er^{3+} nanoprisms. The fabricated $NaYF_4$:Yb^{3+}, Er^{3+} nanoprisms have a uniform hexagonal prism structure with good monodispersity and well-defined facets. The nanoprisms had an average size of 550 nm in diameter and 600 nm in height.

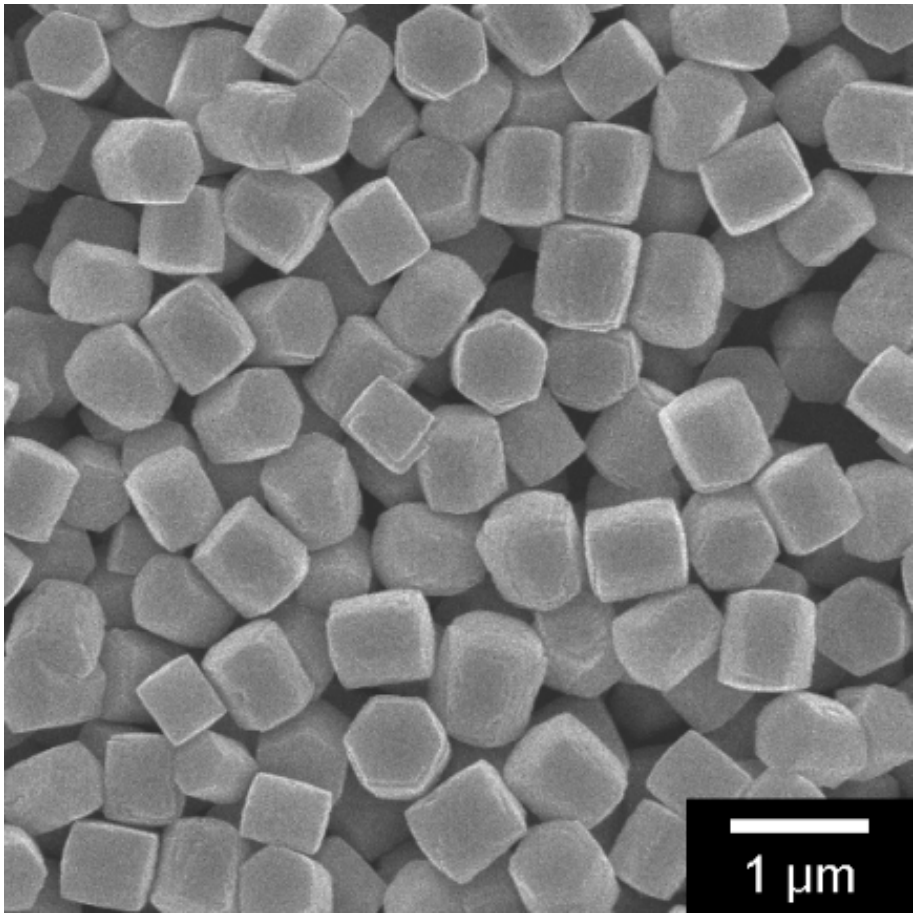

Figure 22. SEM image of $NaYF_4$:Yb^{3+}, Er^{3+} hexagonal nanoprisms

3.2.2 Characterization of β-$NaYF_4$:Yb^{3+}, Er^{3+} hexagonal nanoprisms

The crystallinity of the $NaYF_4$:Yb^{3+}, Er^{3+} nanoprisms was confirmed by X-ray diffraction (XRD), as shown in **figure 23**. The diffraction peaks of the $NaYF_4$:Yb^{3+}, Er^{3+} nanoprisms corresponded exactly to the pure crystalline hexagonal β-$NaYF_4$ phase (JCPDS No. 16-0334). Compared with the cubic α-$NaYF_4$ phase, hexagonal β-$NaYF_4$ is a more efficient host lattice of various lanthanide ions for upconversion PL, due to its high upconversion quantum yield.[113]

Figure 24 shows the upconversion PL spectrum of $NaYF_4$:Yb^{3+}, Er^{3+} nanoprisms under 980-nm excitation. In the upconversion process of the $NaYF_4$:Yb^{3+}, Er^{3+} system, the energy in Yb^{3+} excited by NIR light is transferred to Er^{3+} ions and released as high-energy visible light. Four Er^{3+} emission peaks at 408, 523, 543, and 655 nm were observed; these peaks were assigned to $^2H_{9/2} \rightarrow {}^4I_{15/2}$ (408 nm), $^2H_{11/2} \rightarrow {}^4I_{15/2}$ (523 nm), $^4S_{3/2} \rightarrow {}^4I_{15/2}$ (543 nm), and $^4F_{9/2} \rightarrow {}^4I_{15/2}$ (655 nm) transitions (**Figure 25**).[113] Notably, the $^4S_{3/2} \rightarrow {}^4I_{15/2}$ transition, a dominant peak in the emission spectrum of $NaYF_4$:Yb^{3+}, Er^{3+} nanoprisms, corresponds to bright green fluorescence under 980 nm

excitation (**Fig. 26**). This result suggests that the $NaYF_4:Yb^{3+}$, Er^{3+} nanoprisms facilitate NIR light absorption by the perovskite sensitizer as upconversion PL, broadening the absorption spectrum range of the PSC device.

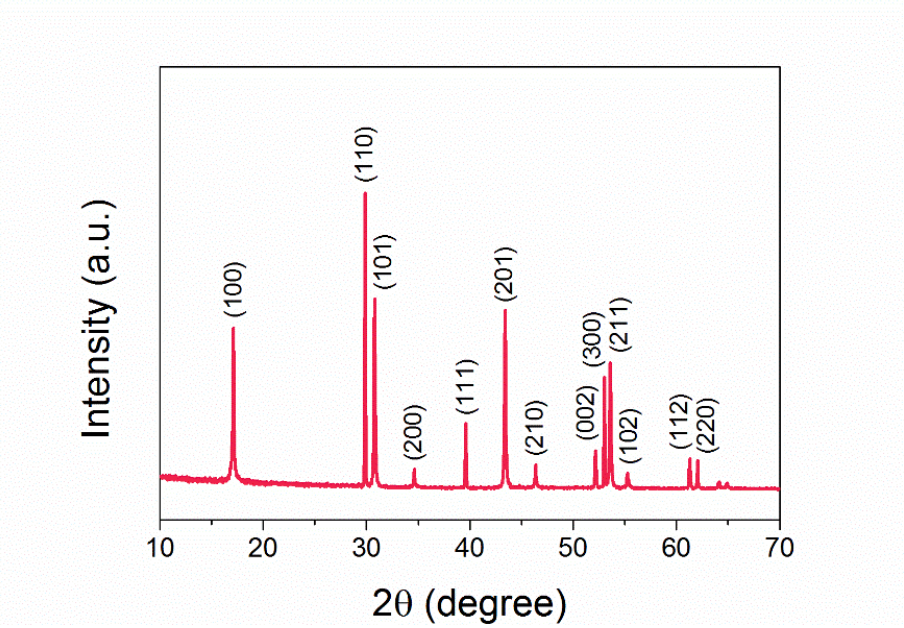

Figure 23. XRD pattern of $NaYF_4$:Yb^{3+}, Er^{3+} hexagonal nanoprisms

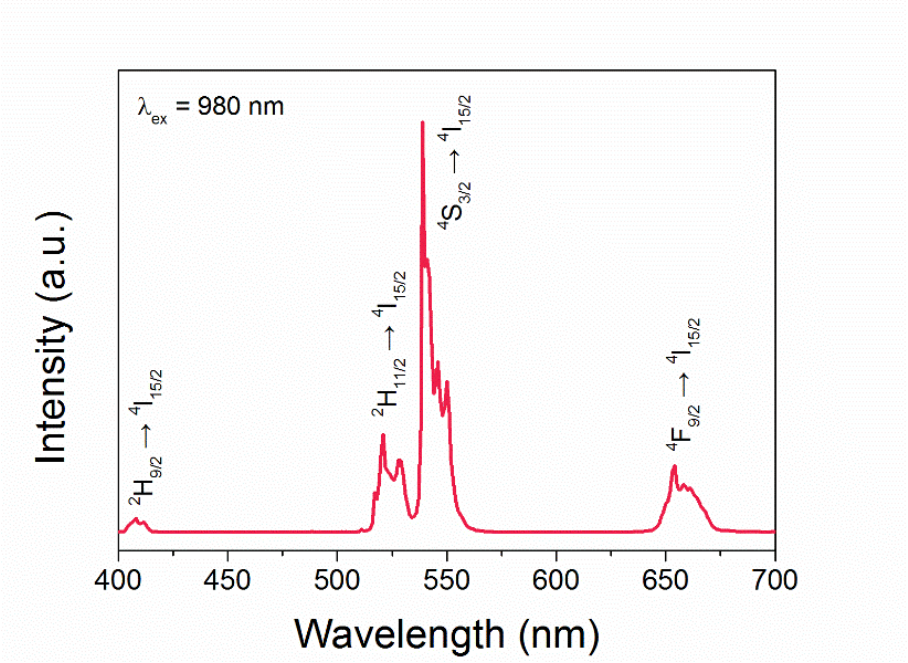

Figure 24. Upconversion photoluminescence (PL) spectrum of $NaYF_4:Yb^{3+}$, Er^{3+} hexagonal nanoprisms under 980nm NIR laser excitation.

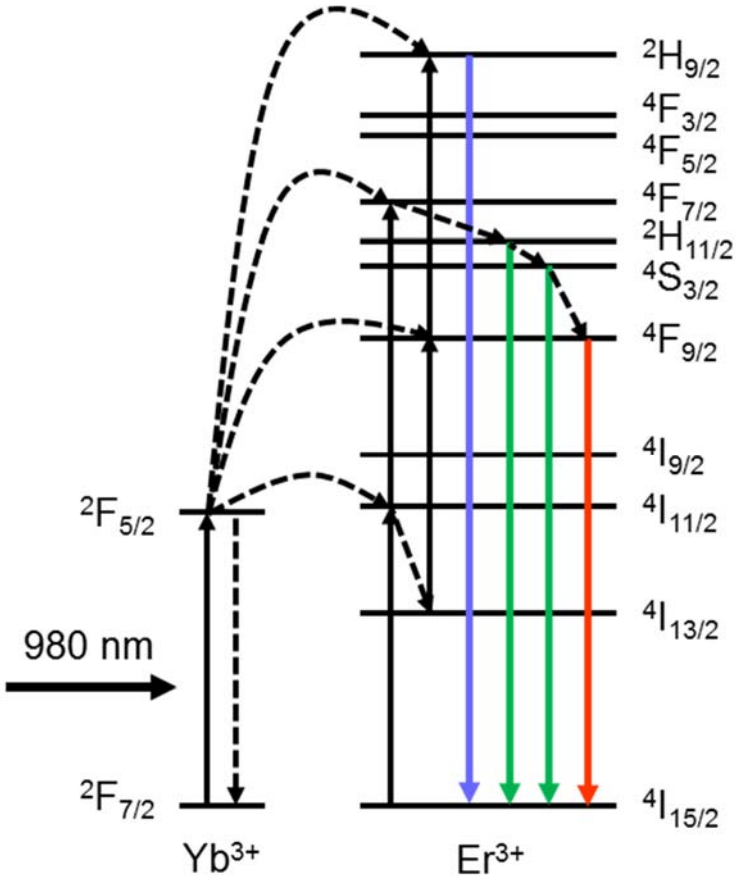

Figure 25. Detailed energy-level diagram and corresponding energy transitions in the $NaYF_4$:Yb^{3+}, Er^{3+} system.

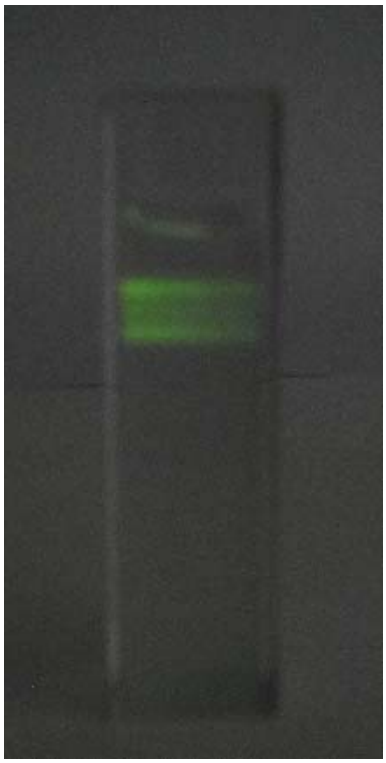

Figure 26. Digital photograph of $NaYF_4:Yb^{3+}$, Er^{3+} hexagonal nanoprisms under 980 nm NIR laser excitation.

3.2.3 Application to perovskite solar cells

The upconverting $NaYF_4:Yb^{3+}$, Er^{3+} nanoprisms were introduced to the TiO_2 mesoporous layer in a PSC device as upconverting centers (**Figure 27**) TiO_2 nanoparticle- and $NaYF_4:Yb^{3+}$, Er^{3+} nanoprism-based pastes were prepared by mixing with ethanol, terpineol, ethyl cellulose, and lauric acid. To introduce an upconverting mesoporous layer into the PSC, diluted TiO_2-$NaYF_4:Yb^{3+}$, Er^{3+} mixed paste was spin-coated onto the compact TiO_2 layer and annealed at 500°C for 30 min. Finally, the upconverting mesoporous film was post-treated with aqueous $TiCl_4$ solution and heated at 500°C for 30 min to reduce charge recombination at the perovskite/TiO_2 and perovskite/$NaYF_4:Yb^{3+}$, Er^{3+} interface. The surface morphology of the upconverting mesoporous layer and the cross-section of the PSC with the upconverting mesoporous film are shown in **Figure 28** and **Figure 29**, respectively; in the figures, the thickness of the TiO_2 mesoporous layer is *ca*. 200 nm and large $NaYF_4:Yb^{3+}$, Er^{3+} hexagonal nanoprisms are exposed over the TiO_2 mesoporous layer. The amount of $NaYF_4:Yb^{3+}$, Er^{3+} nanoprisms on the surface of the upconverting mesoporous layer increases with the concentration of $NaYF_4:Yb^{3+}$, Er^{3+} nanoprisms in the mixed paste.

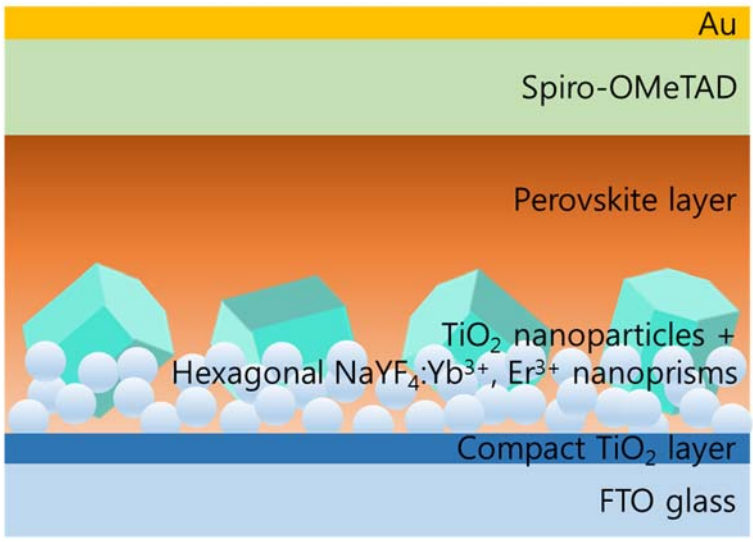

Figure 27. Schematic configuration of the PSC device with a $NaYF_4:Yb^{3+}$, Er^{3+} hexagonal nanoprism upconverting layer.

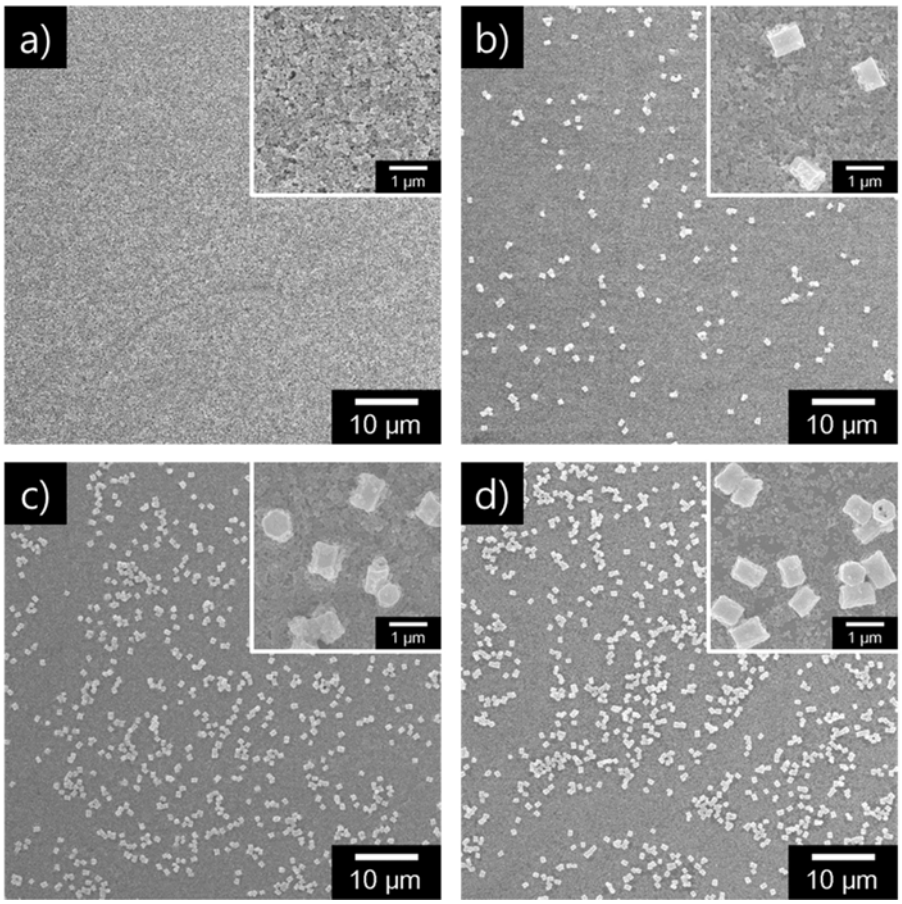

Figure 28. SEM images of TiO_2 mesoporous layer with various $NaYF_4:Yb^{3+}$, Er^{3+} nanoprism concentrations: a) only TiO_2 nanoparticles (reference), b) TiO_2 nanoparticles with 25 wt% $NaYF_4:Yb^{3+}$, Er^{3+} nanoprisms, c) TiO_2 nanoparticles with 50 wt% $NaYF_4:Yb^{3+}$, Er^{3+} nanoprisms, and d) TiO_2 nanoparticles with 75 wt% $NaYF_4:Yb^{3+}$, Er^{3+} nanoprisms.

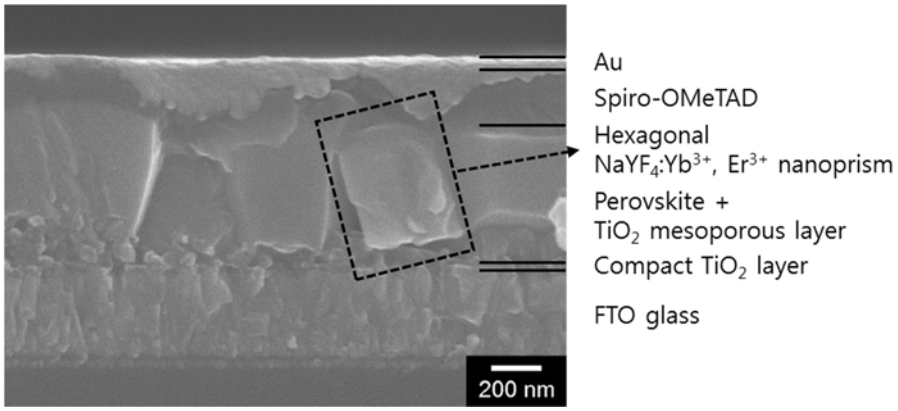

Figure 29. Cross-sectional SEM image of the PSC device with a $NaYF_4:Yb^{3+}$, Er^{3+} hexagonal nanoprism upconverting layer.

The upconverting $NaYF_4:Yb^{3+}$, Er^{3+} nanoprisms are incorporated into the mesoporous layer in $CH_3NH_3PbI_3$ PSCs. To optimize the concentration of $NaYF_4:Yb^{3+}$, Er^{3+} nanoprisms in the mesoporous layer, the photocurrent density–voltage (*J–V*) characteristics of the PSCs with different weight ratios of $NaYF_4:Yb^{3+}$, Er^{3+} nanoprisms in the TiO_2 mesoporous layer were investigated (**Figure 30**); the corresponding photovoltaic properties of the various samples are summarized in **Table 5**. The PSC with the TiO_2 control mesoporous film exhibited a short-circuit current density (J_{sc}) of 18.85 mA cm^{-2} and a PCE (η) of 14.05%. All PSCs with a $NaYF_4:Yb^{3+}$, Er^{3+} nanoprism-added mesoporous layer exhibited enhanced J_{sc} and η, compared with the TiO_2 reference PSC. J_{sc} and η values increased with the amount of $NaYF_4:Yb^{3+}$, Er^{3+} nanoprisms, up to 75 wt% (**Figure 31**). The best performance was obtained using a TiO_2 mesoporous layer with 75 wt% $NaYF_4:Yb^{3+}$, Er^{3+} nanoprisms, demonstrating J_{sc} and η values of 20.23 mA cm^{-2} and 15.98%, respectively. These results represent a 13.74% enhancement in efficiency compared with the TiO_2 reference device. This noticeable enhancement in J_{sc} and η was attributed to the upconversion luminescence properties of the $NaYF_4:Yb^{3+}$, Er^{3+} nanoprisms from

NIR to visible light via the $CH_3NH_3PbI_3$ perovskite layer.

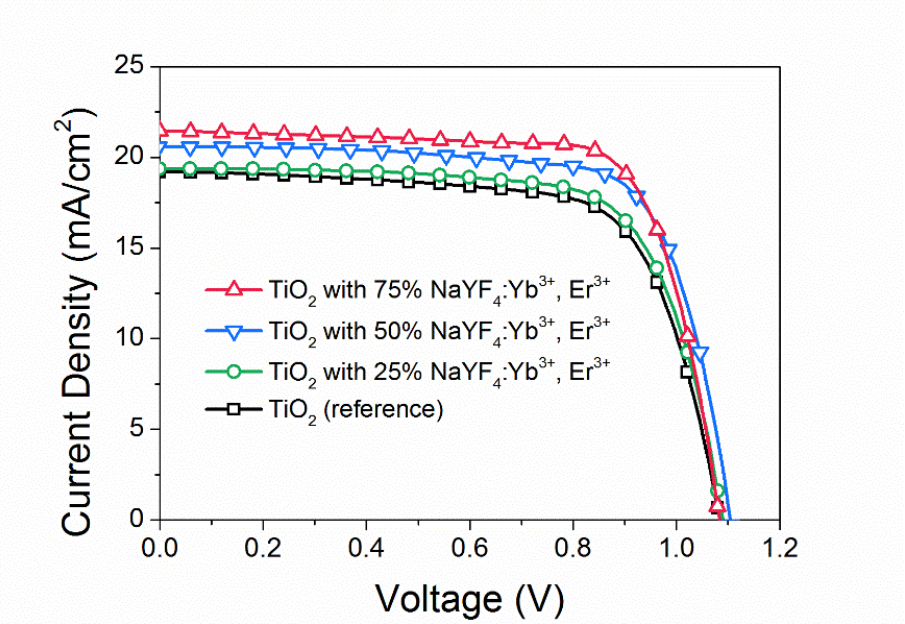

Figure 30. Photocurrent density–voltage (*J–V*) characteristics of PSCs using an upconverting mesoporous layer with varied ratios of $NaYF_4:Yb^{3+}$, Er^{3+} hexagonal nanoprisms.

Table 5. The average photovoltaic parameters of Perovskite solar cells (PSCs) containing $NaYF_4:Yb^{3+}$, Er^{3+} and $NaYF_4$ hexagonal nanoprisms (0, 25, 50 and 75 wt%). Average values of all parameters were obtained for 15 devices.

Devices	J_{sc} (mA cm^{-2})	V_{oc} (V)	*FF*	*PCE (%)*
TiO_2 (Reference)	18.85	1.09	0.68	14.05
TiO_2 with 25% $NaYF_4:Yb^{3+}$, Er^{3+}	19.10	1.10	0.71	15.04
TiO_2 with 50% $NaYF_4:Yb^{3+}$, Er^{3+}	19.95	1.09	0.71	15.51
TiO_2 with 75% $NaYF_4:Yb^{3+}$, Er^{3+}	20.23	1.10	0.72	15.98
TiO_2 with 75% $NaYF_4$	18.52	1.10	0.70	14.26

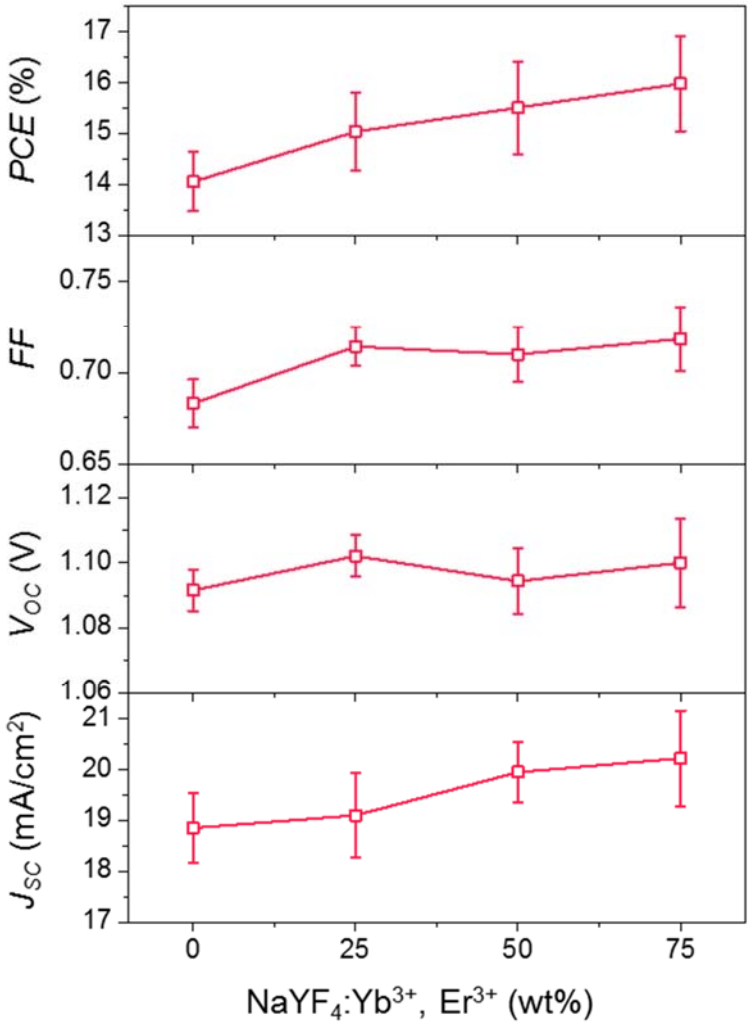

Figure 31. The photovoltaic performance of PSCs using upconverting mesoporous layer with increasing concentration of $NaYF_4:Yb^{3+}$, Er^{3+} hexagonal nanoprisms.

To investigate the charge transfer characteristics in PSC devices, EIS measurements were performed in the frequency range of 1 Hz to 1 MHz at −0.8 V bias under dark conditions. **Figure 32** shows the Nyquist plots of the PSCs for various weight ratios of $NaYF_4$:Yb^{3+}, Er^{3+} nanoprisms in the TiO_2 mesoporous layer. Typically, two semicircles appear in the Nyquist plots in the higher- and lower-frequency regions. The small semicircles at higher frequencies show the charge transfer at the interfaces of the hole transport layer (HTL)/Au electrode; in this case, the semicircles were too small to be distinguished in the Nyquist plots. The large semicircles at lower frequencies are related to the charge recombination of electrons at the mesoporous film/perovskite/HTL interfaces.[114] The recombination resistance values of the fabricated PSCs at the mesoporous film/perovskite/HTL interfaces (R_{ct}) were similar with respect to the various weight ratios of $NaYF_4$:Yb^{3+}, Er^{3+} nanoprisms (**Figure 32**); this implies that there is little charge transfer difference in the TiO_2 layer and TiO_2 layer with $NaYF_4$:Yb^{3+}, Er^{3+} nanoprisms. Thus, the $TiCl_4$ post-treatment that passivates the recombination sites on the upconverting mesoporous layer was believed to be responsible for

reducing charge recombination between the mesoporous film/perovskite interface.[115]

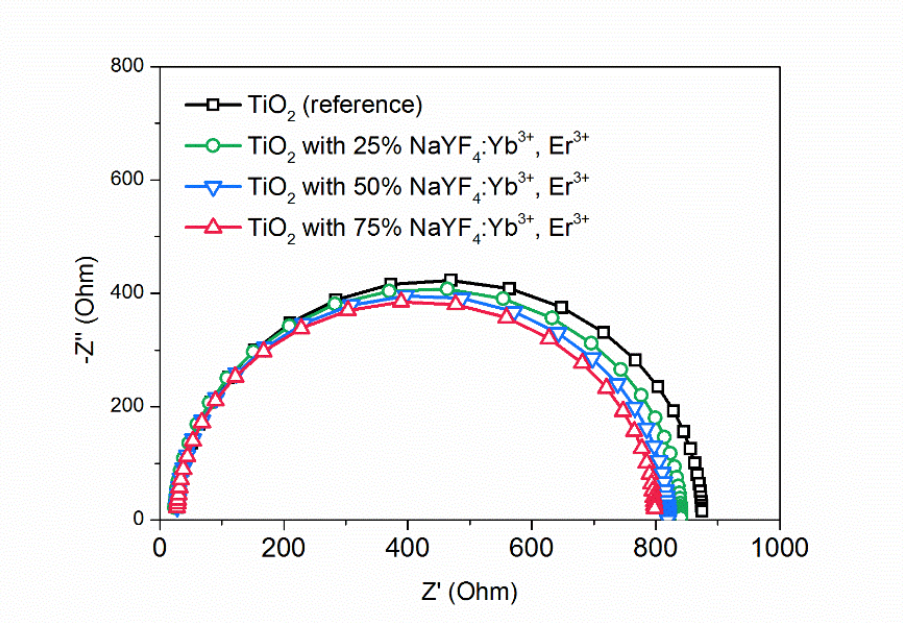

Figure 32. Nyquist plots of PSCs using an upconverting mesoporous layer with varied ratios of $NaYF_4:Yb^{3+}$, Er^{3+} hexagonal nanoprisms. EIS measurements were performed under dark conditions.

To elucidate the NIR photovoltaic capability of $NaYF_4:Yb^{3+}$, Er^{3+} nanoprisms, the optimal photocurrent density–voltage (*J–V*) curves of the PSCs using TiO_2 nanoparticles, TiO_2 nanoparticles with $NaYF_4$ nanoprisms, and TiO_2 nanoparticles with $NaYF_4:Yb^{3+}$, Er^{3+} nanoprisms are presented in **Figure 33**; the associated photovoltaic parameters are listed in **Table 6**. The PSC with $NaYF_4$ nanoprisms in the mesoporous layer exhibited a J_{sc} of 18.52 mA cm^{-2} and a η of 14.26%, similar to the TiO_2 reference device (J_{sc} of 18.85 mA cm^{-2}, η of 14.05%). However, by replacing the $NaYF_4$ nanoprism film with a $NaYF_4:Yb^{3+}$, Er^{3+} nanoprism upconverting layer, J_{sc} increased from 18.52 mA cm^{-2} to 20.23 mA cm^{-2}; Consequentially, the best device performance of 15.98% was achieved, which is a 12.06% enhancement in efficiency compared with the $NaYF_4$ nanoprism control film. **Figure 34** displays IPCE spectra of the PSCs using TiO_2 nanoparticles, TiO_2 nanoparticles with $NaYF_4$ nanoprisms, and TiO_2 nanoparticles with $NaYF_4:Yb^{3+}$, Er^{3+} nanoprisms. A little change was observed in IPCE result when $NaYF_4$ nanoprisms were added in the mesoporous layer. However, The IPCE value over the entire region of 400-750 nm was considerably enhanced with incorporating $NaYF_4:Yb^{3+}$, Er^{3+} nanoprisms in the mesoporous layer. The PSCs

using $NaYF_4:Yb^{3+}$, Er^{3+} nanoprisms exhibits a maximum IPCE value of 85.4% at 525 nm owing to upconversion PL of $NaYF_4:Yb^{3+}$, Er^{3+} nanoprisms. This result is consistent with the photovoltaic performance shown in **Figure 33**. From this perspective, application of $NaYF_4:Yb^{3+}$, Er^{3+} nanoprisms to PSCs represents a way to supplement the energy loss caused by non-absorption of NIR light *via* photon upconversion. When incident light is projected to the PSCs, the visible light is converted into a photocurrent by the perovskite sensitizer. While, NIR photons with energies lower than the bandgap of perovskite (*ca.* 1.55 eV) are effectively converted into visible photons by the $NaYF_4:Yb^{3+}$, Er^{3+} nanoprisms to enhance photovoltaic performance (**Figure 35**).

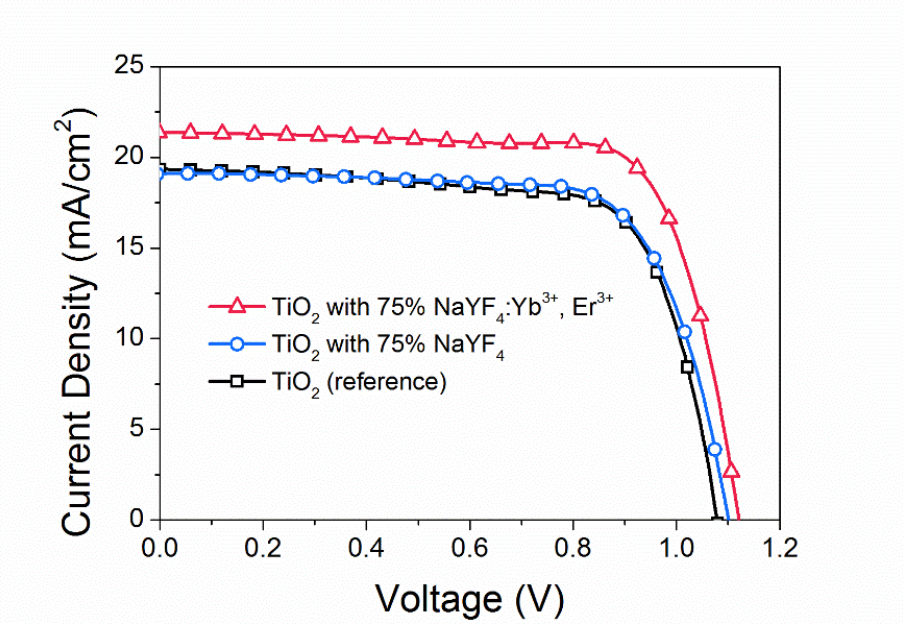

Figure 33. Photocurrent density–voltage (*J–V*) characteristics of PSCs using TiO_2 nanoparticles, $NaYF_4$ hexagonal nanoprisms, and $NaYF_4$:Yb^{3+}, Er^{3+} hexagonal nanoprisms.

Table 6. Photovoltaic parameters of high-performance PSCs using TiO_2 nanoparticles, $NaYF_4$ hexagonal nanoprisms, and $NaYF_4$:Yb^{3+}, Er^{3+} hexagonal nanoprisms. Measurements were performed under AM 1.5G sunlight intensity of 100 W cm^{-2}.

Devices[a]	J_{SC} (mA cm^{-2})	V_{OC} (V)	*FF*	η (%)
TiO_2 (Reference)	19.60	1.09	0.68	14.56
TiO_2 with 75% $NaYF_4$	19.12	1.11	0.71	14.93
TiO_2 with 75% $NaYF_4$:Yb^{3+}, Er^{3+}	21.40	1.13	0.73	17.58

[a] Active area of the fabricated PSC devices is 0.09 cm^2.

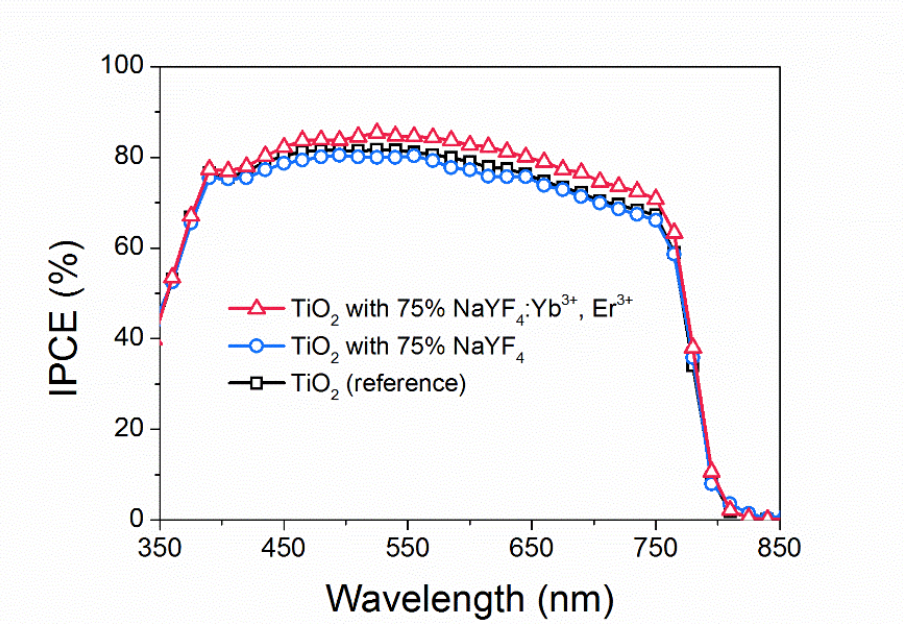

Figure 34. IPCE specta of PSCs using TiO_2 nanoparticles, $NaYF_4$ hexagonal nanoprisms, and $NaYF_4:Yb^{3+}$, Er^{3+} hexagonal nanoprisms.

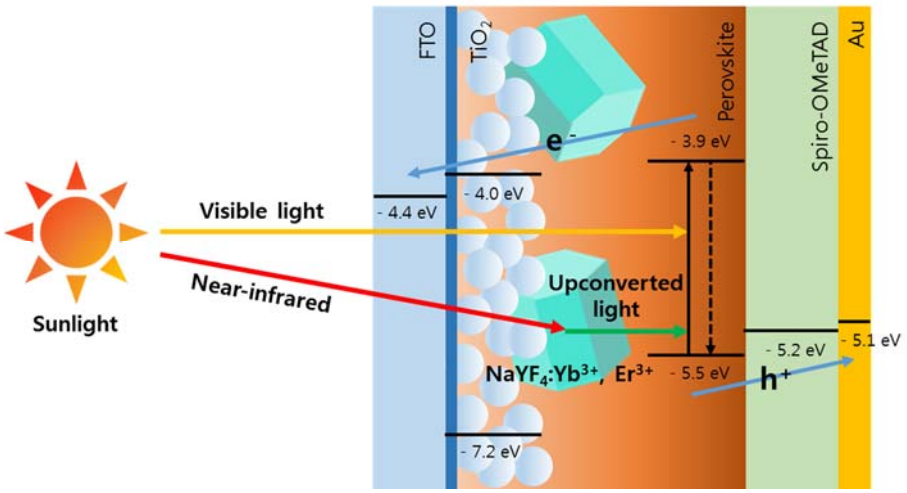

Figure 35. The schematic diagrams of the energy transfer process in PSCs using an upconverting mesoporous layer.

3.3. Size-controlled Ag@SiO_2 nanoplates for perovskite solar cells

3.3.1. Fabrication of size-controlled Ag@SiO_2 nanoplates

Size-controlled Ag nanoprisms were prepared via a seed-mediated growh method. Ag seeds were produced by dissolving trisodium citrate, PSSS and $NaBH_4$ in water, followed by addition of aqueous Ag NO_3 solution dropwisely. Aqueous $AgNO_3$ solution was added into Ag seeds solution, which was reduced by ascorbic acid, resulting in formation of Ag nanoplates. Citrate and PSSS acts as a capping agent as it can selsectively bind to Ag (111) facets and thus effectively block the growth along the vertical axis and only allow extensive growth along the lateral direction.[116]

Figure 36 displays a series of Ag nanoplates obtained using different amount of Ag seed solution. The corresponding UV-vis extinction spectra are shown in **Figure 37**. As the amount of Ag seed decreases in reaction medium, the main LSPR peak of Ag nanoplates are red-shifted. As-synthesized Ag nanoplates with the main LSPR peak at 485 nm, 700 nm, and 815 nm were observed by TEM images (**Figure 38**). Ag nanoplates with 485 nm, 700 nm, and 815 nm extinction have a size of 10-20 nm, 20-30 nm and 50-60 nm, respectively. This result suggests that the LSPR peak is red-shifted as

increasing the size of Ag nanoplates. To coat Ag nanoplates with SiO_2 shell, Ag nanoplates were soaked in the MHA ethanolic solution for surface modification. MHA binds strongly to the silver nanoplate surface presumably via a Ag-S bond and at high surface coverage.[117] Then. SiO_2 shell was coated on the surface of Ag nanoplates by Stöber method with the thickness of 10-25 nm (**Figure 38**).

Figure 36. Digital image of series of as-prepared Ag nanoplates illustrating range of colors obtained.

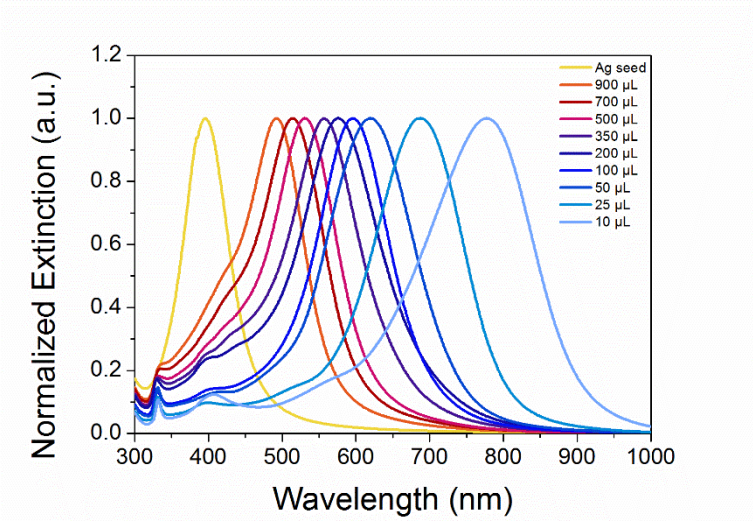

Figure 37. Normalized extinction spectra of series of Ag nanoplates obtained using different volumes of Ag seed solution.

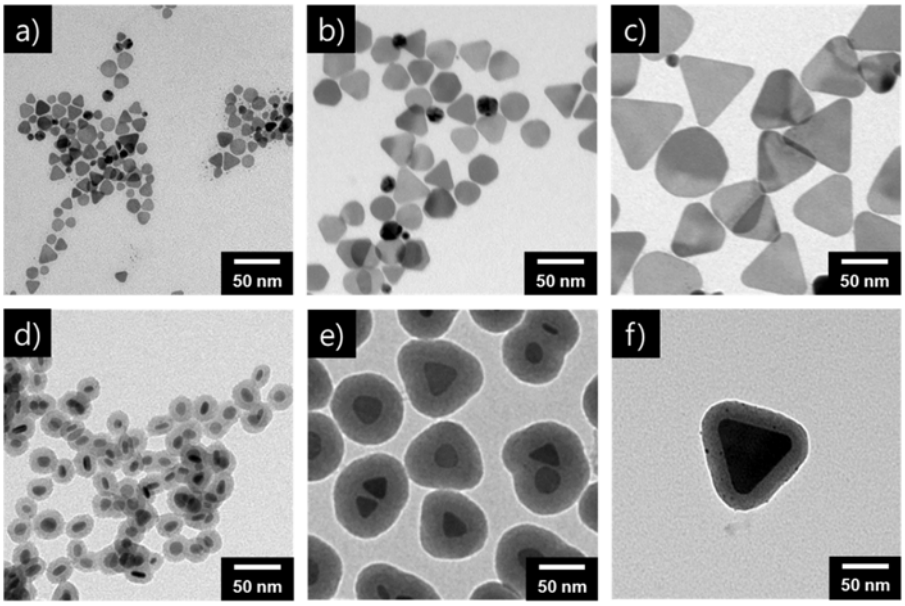

Figure 38. TEM images of as-synthesized Ag nanoplates with the main LSPR peak at a) 485 nm, b) 700 nm, and c) 815 nm. TEM images of silica-coated Ag nanoplatess with the main localized surface plasmon resonance (LSPR) peak at d) 485 nm, e) 700 nm, and f) 815 nm.

3.3.2. Characterization of size-controlled Ag@SiO_2 nanoplates

UV-vis extinction spectra were shown in **Figure 39** to compare the optical properties of the Ag@SiO_2 nanoplates with as-prepared Ag nanoplate. The 45 nm red-shift in the main LSPR band of all Ag nanoprisms was observed after SiO_2 shell coating due to the increase in the local dielectic constant saround the nanoplates.[118] Resultingly, Ag@SiO_2 nanoplates with 530 nm, 745 nm, and 860 nm were prepared. Compared with the absorption spectrum of perovskite film, Ag@SiO_2 nanoplates may contribute the plasmon-induced light absoption in perovskite, especially in visible range (**Figure 40**).

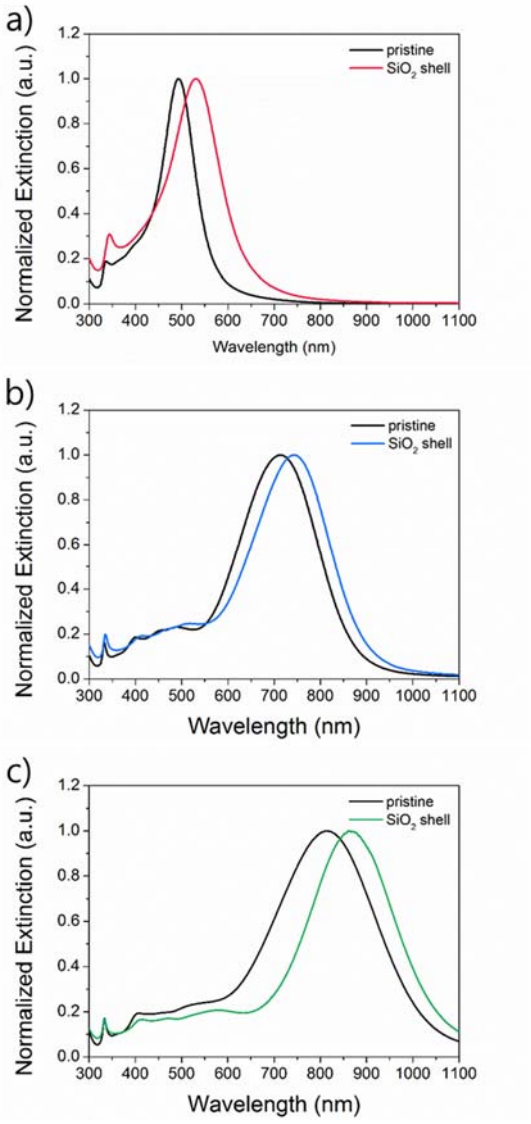

Figure 39. Normailized extinction spectra of Ag@SiO_2 nanoplates before and after silica shell coating with the main LSPR peak at a) 485 nm, b) 700 nm, and c) 815 nm.

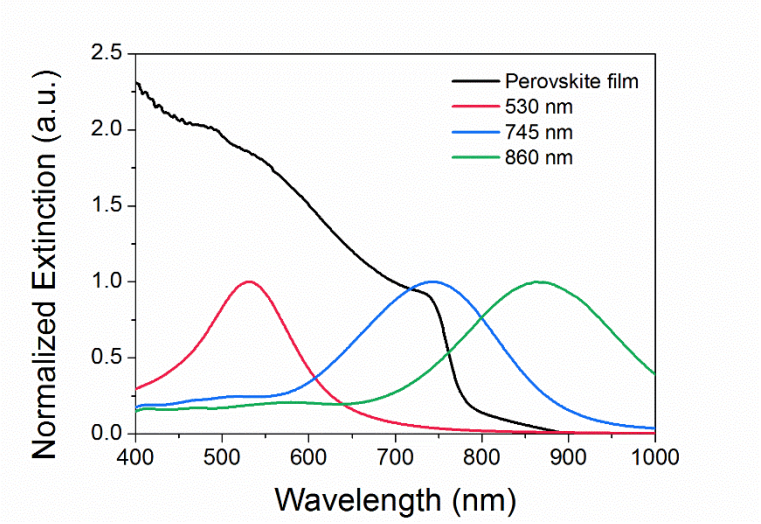

Figure 40. Normailized extinction spectra of perovskite film and Ag@SiO_2 nanoplates with the main LSPR peak at a) 530 nm, b) 745 nm, and c) 860 nm.

3.3.3. Application to perovskite solar cells

The plasmonic $Ag@SiO_2$ nanoplates were introduced to the TiO_2 mesoporous layer in a PSC device (**Figure 40**). The TiO_2 paste was mixed with the $Ag@SiO_2$ nanoplates by ratios ranging from 0.2wt% to 1wt% (with respect to TiO_2 nanoparticles). To incorporate the $Ag@SiO_2$ nanoplates into the PSC, diluted $TiO_2/Ag@SiO_2$ nanoplate paste was spin-coated onto the compact TiO_2 layer and annealed at 500°C for 30 min. Finally, the mesoporous film was post-treated with aqueous $TiCl_4$ solution and heated at 500°C for 30 min. The cross-section of the PSC with the $Ag@SiO_2$ nanoplates is shown in **Figure 42**.

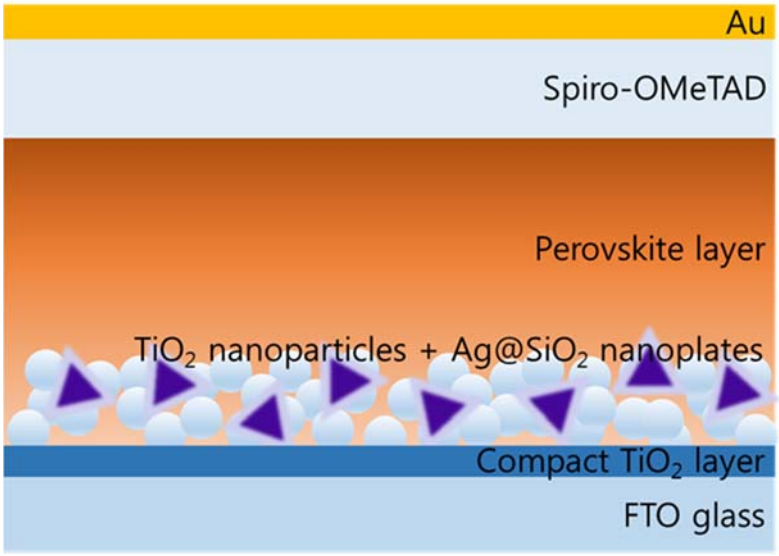

Figure 41. Schematic configuration of the PSC device with size-controlled Ag@SiO_2 nanoplates.

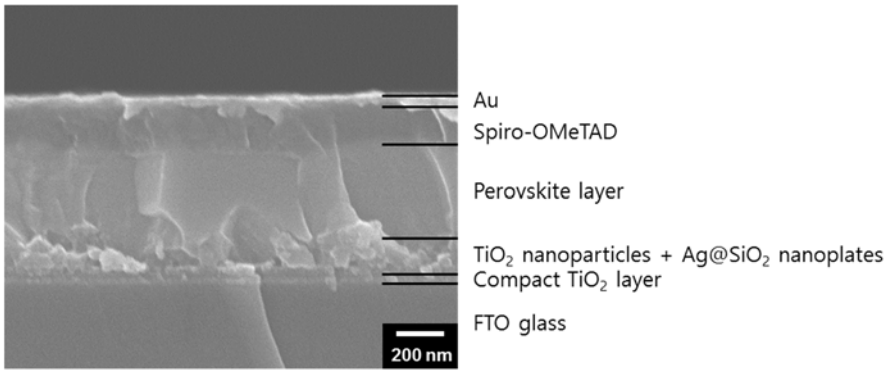

Figure 42. Cross-sectional SEM image of the PSC device with size-controlled Ag@SiO_2 nanoplates.

To optimize the concentration of Ag@SiO_2 nanoplates in the mesoporous layer, the J_{sc} and η of the PSCs with different weight ratios of Ag@SiO_2 nanoplates in the TiO_2 mesoporous layer were investigated (**Figure 43**). With increasing the concentration of Ag@SiO_2 nanoplates in TiO_2 mesoporous layer, J_{sc} and η increased up to 0.6 wt% of Ag, followed by a decrease in J_{sc} and η with further increase in the Ag concentration. The photocurrent density–voltage (*J–V*) curves of the PSCs using TiO_2 nanoparticles and TiO_2 nanoparticles with various Ag@SiO_2 nanoplates are presented in **Figure 44**; the associated photovoltaic parameters are listed in **Table 7**. The best performance was obtained using Ag@SiO_2 nanoplates with a 745 nm extinction an Ag weight ratio of 0.6 wt%, demonstrating J_{sc} and η values of 21.48 mA cm^{-2} and 16.96%, respectively. These results corresponded to a 20.80% enhancement in performance, compared with that of the reference cell. This remarkable enhancement in J_{sc} and η was attributed to the plasmon-enhanced light absorption of Ag@SiO_2 nanoprisms. However, when the Ag concentration in TiO_2 mesoporous layer exceeded 0.6 mol%, a decrease in J_{sc} was observed. This result may be associated with the increased trapping of photogenerated electrons and increased light

absorption by Ag, which transformed part of the incident solar power into heat.[67]

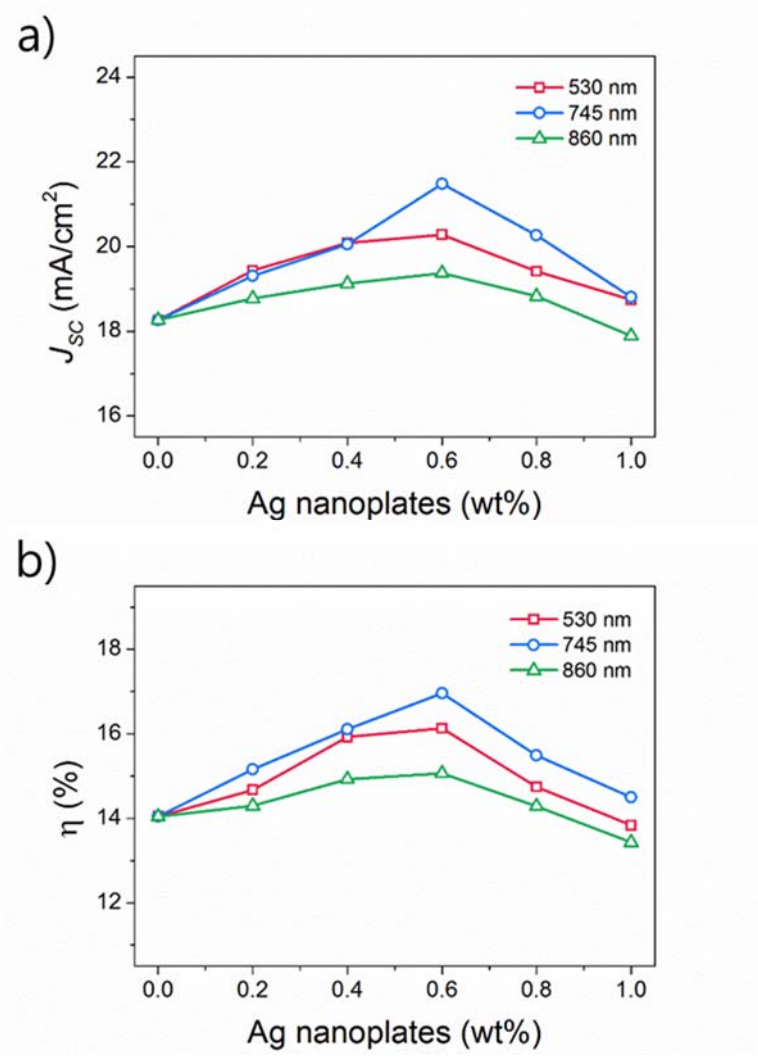

Figure 43. The dependences of a) J_{sc} and b) η on the Ag nanoplates concentration of 0–1 wt% with different LSPR peaks.

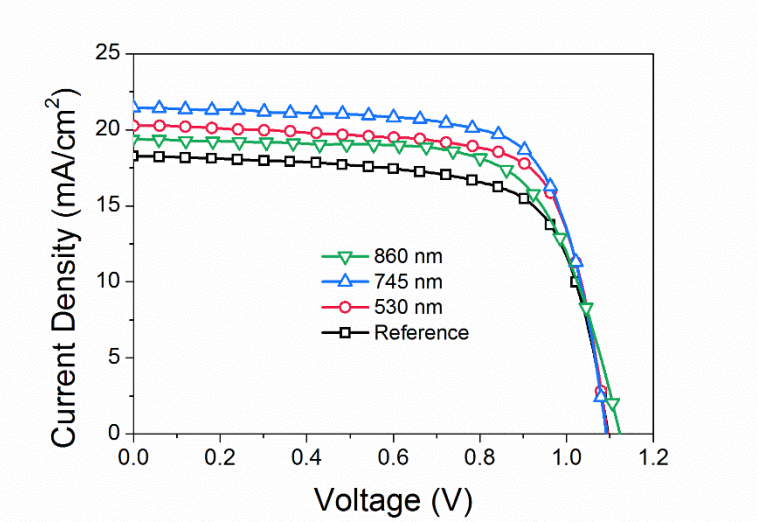

Figure 44. Photocurrent density–voltage (*J*–*V*) characteristics of PSCs using TiO_2 nanoparticles with various Ag@SiO_2 nanoplates (0.6 wt% of Ag).

Table 7. Photovoltaic parameters of PSCs using TiO_2 nanoparticles, with various $Ag@SiO_2$ nanoplates (0.6 wt% of Ag). Measurements were performed under AM 1.5G sunlight intensity of 100 W cm^{-2}.

Devices[a]	J_{SC} (mA cm^{-2})	V_{OC} (V)	*FF*	η (%)
TiO_2 (Reference)	18.27	1.10	0.70	14.04
530 nm extinction	20.28	1.10	0.73	16.13
745 nm extinction	21.48	1.09	0.72	16.96
860 nm extinction	19.38	1.12	0.69	15.07

[a] Active area of the fabricated PSC devices is 0.09 cm^2

To elucidate the photovoltaic capability according to the main LSPR peak of $Ag@SiO_2$ nanoplates, the IPCE spectra were measured from the PSCs using $Ag@SiO_2$ nanoplates with different LSPR peak. **Figure 45a** displays IPCE spectra of the PSCs using TiO_2 nanoparticles, and $Ag@SiO_2$ nanoplates with the 530 nm, 745 nm, and 860 nm extinction. The IPCE value over the entire region of 400-750 nm was considerably enhanced with incorporating $Ag@SiO_2$ nanoplates in the mesoporous layer due to plasmon-enhanced light trapping of $Ag@SiO_2$ nanoplates. This result is consistent with the photovoltaic performance shown in **Figure 44**. The relative intensity of the IPCE spectra of the PSCs including $Ag@SiO_2$ nanoplates with different LSPR extinction were shown in **Figure 45b**. In the relative IPCE improvement factor spectra, the improvement of $Ag@SiO_2$ nanoplates with 745 nm extinction is higher than those with 530 nm extinction over the entire region of 400-750 nm. This result suggests that plasmon-enhanced light absorption in PSCs are maximized when the LSPR peak of $Ag@SiO_2$ nanoplates is near the bandgap of perovskite.[119] While, the intensity of $Ag@SiO_2$ nanoplates with 860 nm extinction is stronger in the low energy region but weaker in the high nergy region. The LSPR below the bandgap of perovskite may

slightly contribute the light absorption near the bandgap of perovskite film.

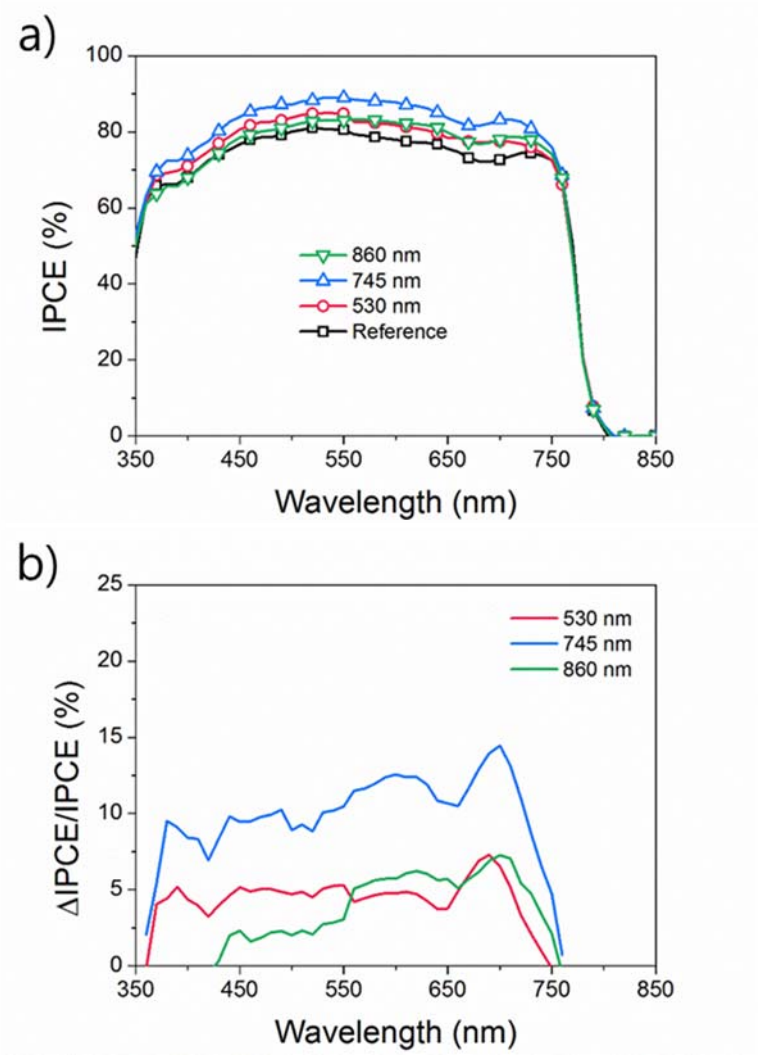

Figure 45. a) IPCE specta of PSCs PSCs using TiO_2 nanoparticles with Ag@SiO_2 nanoplates and b) the relative IPCE improvement factor spectra.

4. CONCLUSIONS

The various light harvesting inorganic nanomaterials including $CeO_2:Eu^{3+}$ nano-octahedra, $NaYF_4:Yb^{3+}$, Er^{3+} hexagonal nanoprisms, and size-controlled $Ag@SiO_2$ nanoplates were successfully prepared. Prepared nanomaterials exhibited improved photovoltaic performance in the solar cell applications due to excellent light harvesting properties. The subtopics could be summerized as follows;

1. Single-crystalline, $CeO_2:Eu^{3+}$ nano-octahedra, successfully prepared using a simple hydrothermal method, were investigated to determine their photovoltaic properties in an effort to enhance the light harvesting efficiency of DSSCs. The size of the $CeO_2:Eu^{3+}$ nano-octahedra (300–400 nm), as well as their mirrorlike facets, significantly improved the diffuse reflectance of visible light. Excitation of the $CeO_2:Eu^{3+}$ nano-octahedron with 330 nm ultraviolet light was re-emitted *via* downconversion PL from 570 to 672 nm, corresponding to the $^5D_0 \rightarrow {}^7F_J$ transition in the Eu^{3+} ions. Downconversion PL was dominant at 590 nm and had a maximum intensity for 1 mol% Eu^{3+}. The $CeO_2:Eu^{3+}$ nano-octahedron-based DSSCs exhibited a PCE of 8.36%, an increase

of 14%, compared with conventional TiO_2 nanoparticle-based DSSCs, due to the strong light-scattering and downconversion PL of the $CeO_2:Eu^{3+}$ nano-octahedra.

2. $NaYF_4:Yb^{3+}$, Er^{3+} hexagonal nanoprisms were fabricated *via* a simple hydrothermal process. The fabricated $NaYF_4:Yb^{3+}$, Er^{3+} nanoprisms have a uniform hexagonal prism structure (an average size of 550 nm in diameter and 600 nm in height) with good monodispersity and well-defined facets. The XRD peaks of the $NaYF_4:Yb^{3+}$, Er^{3+} nanoprisms corresponded exactly to the pure crystalline hexagonal β-$NaYF_4$ phase. Under a 980 nm excitation, Four Er^{3+} emission peaks at 408, 523, 543, and 655 nm were observed. Notably, the $^4S_{3/2} \rightarrow {}^4I_{15/2}$ transition, a dominant peak in the emission spectrum of $NaYF_4:Yb^{3+}$, Er^{3+} nanoprisms, corresponds to bright green fluorescence. $NaYF_4:Yb^{3+}$, Er^{3+} nanoprisms were introduced to the TiO_2 mesoporous layer in a PSC device as upconverting centers. The PSC with a $NaYF_4:Yb^{3+}$, Er^{3+} nanoprisms exhibited the highest PCE of 15.98%, an overall enhancement of 12.06% compared with that of a TiO_2-based PSC device. This enhanced PSC performance was attributed to the outstanding upconversion PL properties of $NaYF_4:Yb^{3+}$, Er^{3+}

nanoprisms.

3. Size-controlled Ag@SiO_2 nanoplates were synthesized using a seed-mediated growth and successive Stöber method. Fabricated Ag nanoplates have the wide LSPR extinction range of 400-900 nm. The 45 nm red-shift in the main LSPR band of all Ag nanoprisms was observed after SiO_2 shell coating due to the increase in the local dielectic constant saround the nanoplates. Size-controlled Ag@SiO_2 nanoplates were incorporated into the TiO_2 mesoporous layer in a PSC device. The PSC using Ag@SiO_2 nanoplates with a 745 nm extinction an Ag weight ratio of 0.6 wt% exhibited the PCE 16.96%, an overall enhancement of 20.80% compared with that of a TiO_2-based PSC device. This enhanced PSC performance was attributed to the excellent plasmon-enhanced light trapping properties of Ag@SiO_2 nanoplates.

References

[1] Q. Zhang, D. Myers, J. Lan, S. A. Jenekhe and G. Cao, *Phys. Chem. Chem. Phys.*, 2012, **14**, 14982.

[2] M. L. Brongersma, Y. Cui and S. Fan, *Nat Mater*, 2014, **13**, 451.

[3] S. H. Hwang, J. Yun and J. Jang, *Adv. Funct. Mater.*, 2014, **24**, 7619.

[4] Y.-C. Park, Y.-J. Chang, B.-G. Kum, E.-H. Kong, J. Y. Son, Y. S. Kwon, T. Park and H. M. Jang, *J. Mater. Chem.*, 2011, **21**, 9582.

[5] S. Dadgostar, F. Tajabadi and N. Taghavinia, *ACS Appl. Mater. Interfaces*, 2012, **4**, 2964.

[6] Z. Dong, X. Lai, J. E. Halpert, N. Yang, L. Yi, J. Zhai, D. Wang, Z. Tang and L. Jiang, *Adv. Mater.*, 2012, **24**, 1046.

[7] W.-T. Jiang, C.-T. Wu, Y.-H. Sung and J.-J. Wu, *ACS Appl. Mater. Interfaces*, 2013, **5**, 911.

[8] K.-N. Li, Y.-F. Wang, Y.-F. Xu, H.-Y. Chen, C.-Y. Su and D.-B. Kuang, *ACS Appl. Mater. Interfaces*, 2013, **5**, 5105.

[9] J. Qian, P. Liu, Y. Xiao, Y. Jiang, Y. Cao, X. Ai and H. Yang, *Adv. Mater.*, 2009, **21**, 3663.

[10] H. Yu, Y. Bai, X. Zong, F. Tang, G. Q. M. Lu and L. Wang, *Chem. Commun.*, 2012, **48**, 7386.

[11] S. H. Hwang, D. H. Shin, J. Yun, C. Kim, M. Choi and J. Jang, *Chem. Eur. J.*, 2014, **20**, 4439.

[12] W. Peng and L. Han, *J. Mater. Chem.*, 2012, **22**, 20773.

[13] S. H. Hwang, J. Roh and J. Jang, *Chem. Eur. J.*, 2013, **19**, 13120.

[14] S. H. Hwang, C. Kim, H. Song, S. Son and J. Jang, *ACS Appl. Mater. Interfaces*, 2012, **4**, 5287.

[15] E. E. Khawaja, S. M. A. Durrani and M. F. Al-Kuhaili, *J. Phys. D-Appl. Phys.*, 2003, **36**, 545.

[16] G. Cao, *Photonics Spectra*, 2008, **42**, 60.

[17] C. Strümpel, M. McCann, G. Beaucarne, V. Arkhipov, A. Slaoui, V. Švrček, C. del Cañizo and I. Tobias, *Sol. Energy Mater. Sol. Cells*, 2007, **91**, 238.

[18] B. S. Richards, *Sol. Energy Mater. Sol. Cells*, 2006, **90**, 1189.

[19] Q. Y. Zhang and X. Y. Huang, *Progress in Materials Science*, 2010, **55**, 353.

[20] W. G. J. H. M. v. Sark, K. W. J. Barnham, L. H. Slooff, A. J. Chatten, A. Büchtemann, A. Meyer, S. J. McCormack, R. Koole, D. J. Farrell, R. Bose, E. E. Bende, A. R. Burgers, T. Budel, J. Quilitz, M. Kennedy, T. Meyer, C. D. M. Donegá, A. Meijerink and D. Vanmaekelbergh, *Opt. Express*, 2008, **16**, 21773.

[21] B. M. van der Ende, L. Aarts and A. Meijerink, *Phys. Chem. Chem. Phys.*, 2009, **11**, 11081.

[22] M. G. Debije and P. P. C. Verbunt, *Adv. Energy Mater.*, 2012, **2**, 12.

[23] R. Reisfeld, *Opt. Mater.*, 2010, **32**, 850.

[24] M. Méndez, Y. Cesteros, L. F. Marsal, E. Martínez-Ferrero, P. Salagre, P. Formentín, J. Pallarès, M. Aguiló, F. Díaz and J. J. Carvajal, *Opt. Mater.*, 2011, **33**, 1120.

[25] W. Xu, H. Song, D. Yan, H. Zhu, Y. Wang, S. Xu, X. Bai, B. Dong and Y. Liu, *J. Mater. Chem.*, 2011, **21**, 12331.

[26] J. Wu, G. Xie, J. Lin, Z. Lan, M. Huang and Y. Huang, *J. Power Sources*, 2010, **195**, 6937.

[27] J. Liu, Q. Yao and Y. Li, *Appl. Phys. Lett.*, 2006, **88**, 173119.

[28] S. J. Gallagher, B. Norton and P. C. Eames, *Sol. Energy*, 2007, **81**, 813.

[29] M. Stupca, M. Alsalhi, T. Al Saud, A. Almuhanna and M. H. Nayfeh, *Appl. Phys. Lett.*, 2007, **91**, 063107.

[30] N. Yamada, L. Nguyen Anh and T. Kambayashi, *Sol. Energy Mater. Sol. Cells*, 2010, **94**, 413.

[31] M. J. Currie, J. K. Mapel, T. D. Heidel, S. Goffri and M. A. Baldo,

Science, 2008, **321**, 226.

[32] J. Ovenstone, P. J. Titler, R. Withnall and J. Silver, *J. Phys. Chem. B*, 2001, **105**, 7170.

[33] J.-W. Wang, Y.-M. Chang, H.-C. Chang, S.-H. Lin, L. C. L. Huang, X.-L. Kong and M.-W. Kang, *Chem. Phys. Lett.*, 2005, **405**, 314.

[34] Y. Liu, D. Tu, H. Zhu, R. Li, W. Luo and X. Chen, *Adv. Mater.*, 2010, **22**, 3266.

[35] R. Sankara and G. V. Subba Rao, *J. Electrochem. Soc.*, 2000, **147**, 2773.

[36] M. Oikawa and S. Fujihara, *J. Eur. Ceram. Soc.*, 2005, **25**, 2921.

[37] X. Liu, S. Chen and X. Wang, *J. Lumines.*, 2007, **127**, 650.

[38] S. Fujihara and M. Oikawa, *J. Appl. Phys.*, 2004, **95**, 8002.

[39] T. Trupke, M. A. Green and P. Würfel, *J. Appl. Phys.*, 2002, **92**, 1668.

[40] G. Chen, C. Yang and P. N. Prasad, *Acc. Chem. Res.*, 2013, **46**, 1474.

[41] F. Auzel, *Chem. Rev.*, 2004, **104**, 139.

[42] J. de Wild, A. Meijerink, J. K. Rath, W. G. J. H. M. van Sark and R. E. I. Schropp, *Energy Environ. Sci.*, 2011, **4**, 4835.

[43] E. L. Cates, S. L. Chinnapongse, J.-H. Kim and J.-H. Kim, *Environ. Sci. Technol.*, 2012, **46**, 12316.

[44] H.-Q. Wang, M. Batentschuk, A. Osvet, L. Pinna and C. J. Brabec, *Adv. Mater.*, 2011, **23**, 2675.

[45] A. Shalav, B. S. Richards and M. A. Green, *Sol. Energy Mater. Sol. Cells*, 2007, **91**, 829.

[46] T. Trupke, M. A. Green and P. Würfel, *J. Appl. Phys.*, 2002, **92**, 4117.

[47] A. C. Atre and J. A. Dionne, *J. Appl. Phys.*, 2011, **110**, 034505.

[48] R. Scheps, *Prog. Quantum Electron.*, 1996, **20**, 271.

[49] A. J. Silversmith, W. Lenth and R. M. Macfarlane, *Appl. Phys. Lett.*, 1987, **51**, 1977.

[50] A. Shalav, B. S. Richards, T. Trupke, K. W. Krämer and H. U. Güdel, *Appl. Phys. Lett.*, 2005, **86**, 013505.

[51] L. Liang, Y. Liu and X.-Z. Zhao, *Chem. Commun.*, 2013, **49**, 3958.

[52] X. Niu, H. Chen, Y. Wang, W. Wang, X. Sun and L. Chen, *ACS Appl. Mater. Interfaces*, 2014, **6**, 5152.

[53] Z. Wei, L. Sun, J. Liu, J. Z. Zhang, H. Yang, Y. Yang and L. Shi, *Biomaterials*, 2014, **35**, 387.

[54] J. C. Goldschmidt and S. Fischer, *Advanced Optical Materials*, 2015, **3**, 510.

[55] L. Liang, Y. Liu, C. Bu, K. Guo, W. Sun, N. Huang, T. Peng, B. Sebo, M. Pan, W. Liu, S. Guo and X.-Z. Zhao, *Adv. Mater.*, 2013, **25**, 2174.

[56] G.-B. Shan, H. Assaaoudi and G. P. Demopoulos, *ACS Appl. Mater. Interfaces*, 2011, **3**, 3239.

[57] Z. Zhou, J. Wang, F. Nan, C. Bu, Z. Yu, W. Liu, S. Guo, H. Hu and X.-Z. Zhao, *Nanoscale*, 2014, **6**, 2052.

[58] A. Sedlmeier and H. H. Gorris, *Chem. Soc. Rev.*, 2015, **44**, 1526.

[59] P. Mulvaney, *Langmuir*, 1996, **12**, 788.

[60] K. L. Kelly, E. Coronado, L. L. Zhao and G. C. Schatz, *J. Phys. Chem. B*, 2003, **107**, 668.

[61] B. J. Wiley, S. H. Im, Z.-Y. Li, J. McLellan, A. Siekkinen and Y. Xia, *J. Phys. Chem. B*, 2006, **110**, 15666.

[62] H. A. Atwater and A. Polman, *Nat Mater*, 2010, **9**, 205.

[63] J. Mertz, *J. Opt. Soc. Am. B*, 2000, **17**, 1906.

[64] K. R. Catchpole and A. Polman, *Opt. Express*, 2008, **16**, 21793.

[65] J.-L. Wu, F.-C. Chen, Y.-S. Hsiao, F.-C. Chien, P. Chen, C.-H. Kuo, M. H. Huang and C.-S. Hsu, *ACS Nano*, 2011, **5**, 959.

[66] J. Yang, J. You, C.-C. Chen, W.-C. Hsu, H.-r. Tan, X. W. Zhang, Z. Hong and Y. Yang, *ACS Nano*, 2011, **5**, 6210.

[67] J. Qi, X. Dang, P. T. Hammond and A. M. Belcher, *ACS Nano*, 2011, **5**, 7108.

[68] C. Hägglund, M. Zäch, G. Petersson and B. Kasemo, *Appl. Phys. Lett.*, 2008, **92**, 053110.

[69] J. E. Millstone, S. J. Hurst, G. S. Métraux, J. I. Cutler and C. A. Mirkin, *Small*, 2009, **5**, 646.

[70] I. Pastoriza-Santos and L. M. Liz-Marzan, *J. Mater. Chem.*, 2008, **18**, 1724.

[71] G. S. Métraux and C. A. Mirkin, *Adv. Mater.*, 2005, **17**, 412.

[72] R. Jin, Y. Cao, C. A. Mirkin, K. L. Kelly, G. C. Schatz and J. G. Zheng, *Science*, 2001, **294**, 1901.

[73] W. Shi and Z. Ma, *Biosens. Bioelectron.*, 2010, **26**, 1098.

[74] Y. C. Cao, R. Jin and C. A. Mirkin, *Science*, 2002, **297**, 1536.

[75] A. Parfenov, I. Gryczynski, J. Malicka, C. D. Geddes and J. R. Lakowicz, *J. Phys. Chem. B*, 2003, **107**, 8829.

[76] K. A. Homan, M. Souza, R. Truby, G. P. Luke, C. Green, E. Vreeland and S. Emelianov, *ACS Nano*, 2012, **6**, 641.

[77] B. O'Regan and M. Gratzel, *Nature*, 1991, **353**, 737.

[78] M. Gratzel, *Nature*, 2001, **414**, 338.

[79] M. Grätzel, *J. Photochem. Photobiol. C-Photochem. Rev.*, 2003, **4**, 145.

[80] M. Grätzel, *Inorg. Chem.*, 2005, **44**, 6841.

[81] S. Hore, C. Vetter, R. Kern, H. Smit and A. Hinsch, *Sol. Energy Mater. Sol. Cells*, 2006, **90**, 1176.

[82] A. Hagfeldt, G. Boschloo, L. Sun, L. Kloo and H. Pettersson, *Chem. Rev.*, 2010, **110**, 6595.

[83] B. E. Hardin, H. J. Snaith and M. D. McGehee, *Nat Photon*, 2012, **6**, 162.

[84] M. A. Green, A. Ho-Baillie and H. J. Snaith, *Nat Photon*, 2014, **8**, 506.

[85] J. H. Heo, S. H. Im, J. H. Noh, T. N. Mandal, C.-S. Lim, J. A. Chang, Y. H. Lee, H.-j. Kim, A. Sarkar, K. NazeeruddinMd, M. Gratzel and S. I. Seok, *Nat Photon*, 2013, **7**, 486.

[86] S. D. Stranks, G. E. Eperon, G. Grancini, C. Menelaou, M. J. P.

Alcocer, T. Leijtens, L. M. Herz, A. Petrozza and H. J. Snaith, *Science*, 2013, **342**, 341.

[87] G. Xing, N. Mathews, S. Sun, S. S. Lim, Y. M. Lam, M. Grätzel, S. Mhaisalkar and T. C. Sum, *Science*, 2013, **342**, 344.

[88] S. H. Hwang, J. Roh, J. Lee, J. Ryu, J. Yun and J. Jang, *Journal of Materials Chemistry A*, 2014, **2**, 16429.

[89] J. Yun, J. Ryu, J. Lee, H. Yu and J. Jang, *Journal of Materials Chemistry A*, 2016, **4**, 1306.

[90] K. Lee, C.-M. Yoon, J. Noh and J. Jang, *Chem. Commun.*, 2016, **52**, 4231.

[91] H.-S. Kim, C.-R. Lee, J.-H. Im, K.-B. Lee, T. Moehl, A. Marchioro, S.-J. Moon, R. Humphry-Baker, J.-H. Yum, J. E. Moser, M. Grätzel and N.-G. Park, *Sci. Rep.*, 2012, **2**, 591.

[92] W. S. Yang, J. H. Noh, N. J. Jeon, Y. C. Kim, S. Ryu, J. Seo and S. I. Seok, *Science*, 2015, **348**, 1234.

[93] N. J. Jeon, J. H. Noh, Y. C. Kim, W. S. Yang, S. Ryu and S. I. Seok, *Nat Mater*, 2014, **13**, 897.

[94] N. Ahn, D.-Y. Son, I.-H. Jang, S. M. Kang, M. Choi and N.-G. Park, *J. Am. Chem. Soc.*, 2015, **137**, 8696.

[95] N. J. Jeon, J. H. Noh, W. S. Yang, Y. C. Kim, S. Ryu, J. Seo and S. I. Seok, *Nature*, 2015, **517**, 476.

[96] Y. Chen, B. Li, W. Huang, D. Gao and Z. Liang, *Chem. Commun.*, 2015, **51**, 11997.

[97] X. Li, M. Ibrahim Dar, C. Yi, J. Luo, M. Tschumi, S. M. Zakeeruddin, M. K. Nazeeruddin, H. Han and M. Grätzel, *Nat Chem*, 2015, **7**, 703.

[98] J. P. Correa Baena, L. Steier, W. Tress, M. Saliba, S. Neutzner, T. Matsui, F. Giordano, T. J. Jacobsson, A. R. Srimath Kandada, S. M. Zakeeruddin, A. Petrozza, A. Abate, M. K. Nazeeruddin, M. Gratzel and A. Hagfeldt, *Energy Environ. Sci.*, 2015, **8**, 2928.

[99] J.-Y. Jeng, K.-C. Chen, T.-Y. Chiang, P.-Y. Lin, T.-D. Tsai, Y.-C. Chang, T.-F. Guo, P. Chen, T.-C. Wen and Y.-J. Hsu, *Adv. Mater.*, 2014, **26**, 4107.

[100] G. E. Eperon, S. D. Stranks, C. Menelaou, M. B. Johnston, L. M. Herz and H. J. Snaith, *Energy Environ. Sci.*, 2014, **7**, 982.

[101] J.-H. Im, I.-H. Jang, N. Pellet, M. Grätzel and N.-G. Park, *Nat. Nanotechnol.*, 2014, **9**, 927.

[102] K. Wojciechowski, M. Saliba, T. Leijtens, A. Abate and H. J. Snaith, *Energy Environ. Sci.*, 2014, **7**, 1142.

[103] L. Yan, R. Yu, J. Chen and X. Xing, *Cryst. Growth Des.*, 2008, **8**, 1474.

[104] X.-H. Liao, J.-M. Zhu, J.-J. Zhu, J.-Z. Xu and H.-Y. Chen, *Chem. Commun.*, 2001, DOI: 10.1039/B101004M, 937.

[105] S. Tsunekawa, R. Sahara, Y. Kawazoe and K. Ishikawa, *Appl. Surf. Sci.*, 1999, **152**, 53.

[106] H. Zhang, Y. Han, X. Liu, P. Liu, H. Yu, S. Zhang, X. Yao and H. Zhao, *Chem. Commun.*, 2010, **46**, 8395.

[107] A. J. Kenyon, *Prog. Quantum Electron.*, 2002, **26**, 225.

[108] J. Wu, J. Wang, J. Lin, Y. Xiao, G. Yue, M. Huang, Z. Lan, Y. Huang, L. Fan, S. Yin and T. Sato, *Sci. Rep.*, 2013, **3**, 2058.

[109] J. W. Stouwdam and F. C. J. M. van Veggel, *Nano Lett.*, 2002, **2**, 733.

[110] D. Kuang, S. Ito, B. Wenger, C. Klein, J.-E. Moser, R. Humphry-Baker, S. M. Zakeeruddin and M. Grätzel, *J. Am. Chem. Soc.*, 2006, **128**, 4146.

[111] R. Kydd, J. Scott, W. Y. Teoh, K. Chiang and R. Amal, *Langmuir*, 2009, **26**, 2099.

[112] J. van de Lagemaat, N. G. Park and A. J. Frank, *J. Phys. Chem. B*, 2000, **104**, 2044.

[113] C. Li, Z. Quan, J. Yang, P. Yang and J. Lin, *Inorg. Chem.*, 2007, **46**, 6329.

[114] J. Zhang, Z. Hu, L. Huang, G. Yue, J. Liu, X. Lu, Z. Hu, M. Shang, L. Han and Y. Zhu, *Chem. Commun.*, 2015, **51**, 7047.

[115] M. Law, L. E. Greene, A. Radenovic, T. Kuykendall, J. Liphardt and P. Yang, *J. Phys. Chem. B*, 2006, **110**, 22652.

[116] D. Aherne, D. M. Ledwith, M. Gara and J. M. Kelly, *Adv. Funct. Mater.*, 2008, **18**, 2005.

[117] C. Xue, X. Chen, S. J. Hurst and C. A. Mirkin, *Adv. Mater.*, 2007, **19**, 4071.

[118] M. K. Gangishetty, K. E. Lee, R. W. J. Scott and T. L. Kelly, *ACS Appl. Mater. Interfaces*, 2013, **5**, 11044.

[119] G. Chen, J. Seo, C. Yang and P. N. Prasad, *Chem. Soc. Rev.*, 2013, **42**, 8304.

국문초록

에너지에 대한 세계적 수요가 증가함에 때라, 태양전지는 깨끗하고 재생가능한 에너지원으로 인식되어왔다. 태양전지는 태양광을 깨끗한 전기에너지로 효과적으로 변환할수 있어 사실상 지속가능하고 환경친화적인 에너지를 무한정 공급할 수 있다. 나노물질은 비싸지 않은 물질과 넓은 스펙트럼 범위의 광자 에너지를 효과적으로 포획하고, 이를 빠르게 전하 수송체로 분리하고 수집함으로써 태양광을 수확하는 공정 기술을 활용할 수 있게 해줌으로써 높은 태양에너지 변환 효율을 달성할 수 있는 가능성을 열었다. 그러나 반도체의 밴드갭 에너지는 태양전지의 태양에너지 변환 효율에 근본적인 한계값을 지니게 한다. Shockley–Queisser 한계는 1.35 eV로 최적화된 밴드갭을 지닌 반도체 물질에 집광되지 않은 태양광을 조사했을 때 이를 사용한 태양전지의 이론적 최대 효율이 31%로 제한되는 것을 말한다.

본 학위논문에서는 태양전지의 효과적인 광수확을 위한 형태가 제어된 무기 나노소재를 제조하는 것을 기술하였다. $CeO_2:Eu^{3+}$ 나노팔면체는 간단한 수열합성법을 통해 제조하고 이를 염료감응형 태양전지 내 광전극 TiO_2 층에 도입하였다.

만들어진 $CeO_2:Eu^{3+}$ 나노팔면체는 광산란과 하향변환 형광 능력의 이중 기능을 보유하였으며, 염료감응형 태양전지의 광전류 향상을 야기하였다. $NaYF_4:Yb^{3+}$, Er^{3+} 육각 나노기둥은 간단한 수열합성 공정을 통해 제조하였다. $NaYF_4:Yb^{3+}$, Er^{3+} 육각 나노기둥은 페로브스카이트 태양전지의 TiO_2 다공성 층에 상향변환 소자로 도입되었다. 크기가 제어된 은 나노플레이트는 시드 성장법을 통해 제조하고 졸-겔 반응으로 실리카를 나노플레이트 위에 코팅하였다. 페로브스카이트 태양전지에 실리카가 코팅된 은 나노플레이트를 도입하자, 은 나노플레이트의 국소 표면 플라즈몬 공명 현상에 의해 광전류가 현저히 증가하였다.

본 학위논문에 소개된 나노물질은 염료감응형 태양전지, 페로브스카이트 태양전지 및 유기 태양전지 같은 다양한 태양전지 분야에 적용이 가능하다. 또한 본 학위논문은 형태가 제어된 무기 나노입자의 손쉬운 합성 방법을 제공할 뿐만 아니라 고성능 태양전지를 위한 효율적인 광수확에 대한 이해를 제공한다.

주요어: 광흡수; 무기 나노소재; 형태 제어; 태양전지; 염료감응형 태양전지; 페로브스카이트 태양전지

학 번: 2011-24095